

AD-A215 483

1

REPORT DOCUMENTATION PAGE			Form Approved OMB No. 0704-0188	
Public reporting burden for this collection of information is estimated to average 1 hour per response, including the time for reviewing instructions, searching existing data sources, gathering and maintaining the data needed, and completing and reviewing the collection of information. Send comments regarding this burden estimate or any other aspect of this collection of information, including suggestions for reducing this burden, to Washington Headquarters Services, Directorate for Information Operations and Reports, 1215 Jefferson Davis Highway, Suite 1204, Arlington, VA 22202-4302, and to the Office of Management and Budget, Paperwork Reduction Project (0704-0188), Washington, DC 20503.				
AGENCY USE ONLY (Leave blank)	2. REPORT DATE January 1983	3. REPORT TYPE AND DATES COVERED Annual (1/82-12/32)		
4. TITLE AND SUBTITLE VIRTUAL CATHODE THEORY AND DESIGN OF A MILLIMETER WAVE VIRCATOR		5. FUNDING NUMBERS 61102F 2301/A8		
6. AUTHOR(S) D.J. Sullivan, D.E. Voss, W.M. Bollen R.H. Jackson, E.A. Coutsias (UNM)		8. PERFORMING ORGANIZATION REPORT NUMBER AFOSR-TN-89-1517		
7. PERFORMING ORGANIZATION NAME(S) AND ADDRESS(ES) Mission Research Corporation 1720 Randolph Road, S.E. Albuquerque, NM 87106		10. SPONSORING/MONITORING AGENCY REPORT NUMBER F49620-82-C-0014		
9. SPONSORING/MONITORING AGENCY NAME(S) AND ADDRESS(ES) AFOSR BLDG 410 BAFB DC 20332-6448		11. SUPPLEMENTARY NOTES DTIC S ELECTE D DEC 07 1989 B		
12a. DISTRIBUTION/AVAILABILITY STATEMENT Approved for public release; Distribution unlimited.		12b. DISTRIBUTION CODE		
13. ABSTRACT (Maximum 200 words) The theory of a virtual cathode oscillator and detailed experimental design of a millimeter wave virtual cathode oscillator (VIRCATOR) are presented. It is found that second order analytical approximations give an accurate value for the space-charge limiting current of an electron beam in cylindrical geometry. The same Green's function approach could be used on other geometries as well. Exceeding the space-charge limiting current is the necessary condition for virtual electrode formation. However, it does not explain the nature of the space-charge limit instability. The oscillatory stable state of the virtual cathode is found to originate at the bifurcation point of several stable and unstable electron beam states. An analysis of the nonlinear growth rate of the instability is derived. The virtual cathode is in effect a relaxation oscillator. The advantage of the vircator over a reflex klystron is that the virtual cathode moves opposite to the electron beam propagation direction during the bunching phase resulting in enhanced electron densities unobtainable otherwise. The periodic time-dependent nature of the bunching results in efficient microwave generation. Experimental efficiencies of 12% and theoretical efficiencies of 20% have been (over)				
14. SUBJECT TERMS		15. NUMBER OF PAGES 101		
		16. PRICE CODE		
17. SECURITY CLASSIFICATION OF REPORT unclassified	18. SECURITY CLASSIFICATION OF THIS PAGE unclassified	19. SECURITY CLASSIFICATION OF ABSTRACT	20. LIMITATION OF ABSTRACT	

018

obtained. The microwave frequency scales as the relativistic beam plasma frequency. This can be adjusted via an externally applied axial magnetic field. The result is an oscillator which is frequency agile over an order of magnitude without externally changing the physical configuration. Output powers of from kilowatts to gigawatts are obtainable based on the power source. Experimental results are reviewed and explained. The rationale for using a foilless diode as the electron beam source is given. A detailed mechanical and electrical design is described. It entails placing the vircator in a high vacuum vessel with flexibility for further development. The electrical power is pulse formed using a lumped artificial Blumlein line. The axial magnetic field is critically damped for component safety and circuit design simplicity. The beam source is a foilless diode with an annular limiter for collimation and prevention of electrons reflexing into the diode. A W-band (75-110 GHz) microwave grating spectrometer has been designed and constructed for diagnosis of the electromagnetic wave signal. The vircator goal is 1 Megawatt at 100 GHz.

Accession For	
NTIS GRA&I	<input checked="" type="checkbox"/>
DTIC TAB	<input type="checkbox"/>
Unannounced	<input type="checkbox"/>
Justification	
By	
Distribution/	
Availability Codes	
Dist	Avail and/or Special
A-1	

APOSR-TR. 89-1517

ANNUAL REPORT

VIRTUAL CATHODE THEORY AND DESIGN OF A MILLIMETER
WAVE VIRCATOR

Donald J. Sullivan
Donald E. Voss
W. Michael Bollen
Robert H. Jackson
Evangelos A. Coutsias (UNM)

January 1983

Prepared for: Air Force Office of Scientific Research
Physics Directorate
Bolling Air Force Base, DC 20332

Under Contract: F49620-82-C-0014

Prepared by: MISSION RESEARCH CORPORATION
1720 Randolph Road, S.E.
Albuquerque, New Mexico 87106

Approved for public release;
distribution unlimited.

TABLE OF CONTENTS

<u>Section</u>		<u>Page</u>
	ABSTRACT	iv
I	INTRODUCTION	1
II	THE SPACE-CHARGE LIMITING CURRENT	4
III	THE SPACE-CHARGE LIMIT INSTABILITY	17
IV	MICROWAVE GENERATION	40
V	EXPERIMENTAL APPARATUS	56
VI	TECHNICAL REQUIREMENTS AND TASKS	70
	REFERENCES	75
	APPENDIX A: A W-BAND DIFFRACTION GRATING SPECTROMETER	

Approved for Release by NSA on 05-08-2014 pursuant to E.O. 13526
 AUTHORITY: 190-12
 DATE: 11-19-12

Approved for Release by NSA on 05-08-2014 pursuant to E.O. 13526

AIR FORCE OFFICE OF SCIENTIFIC RESEARCH (AFOSR)
 DISTRICT OF COLUMBIA, D.C. 20330-3155
 MATHEMATICS AND PHYSICS DIVISION
 Chief, Technical Information Division

LIST OF ILLUSTRATIONS

<u>Figure</u>		<u>Page</u>
1	Schematic of a relativistic electron beam (REB): (1) cathode; (2) anode; (3) drift space; (4) collector; (5) return current conductor. The principal coordinate axes z , r , and θ are shown.	3
2	Radial cross section of two electron beams. (a) Solid beam where r_0 is the beam radius and k is the drift tube radius. (b) Annular beam where a is the inner radius, b the outer radius, R the drift tube radius and $\epsilon = \frac{b-a}{b}$.	7
3	Plot of v versus γ_a for $\gamma_0 = 5$, $a/R = 0.4$, $b/R = 0.8$. The dashed line results from an approximate second order analytical relation. The points correspond to simulation results. (N.B. γ_a for the point labeled v.c. (virtual cathode) has no physical meaning. It is defined in terms of equation (13)).	16
4	A CCUBE diagnostic of particle kinetic energy versus r for the annular beam showing the radial dependence of γ .	16
5	Schematic of the short-circuited one-dimensional electrostatic diode modelled in this study.	18
6	Electrostatic potential minimum as a function of current, α . The plot depicts the various possible solutions such as normal-C flow (stable), C-overlap (unstable), the partially reflected solution (unstable) and the oscillatory virtual cathode (stable). The motion around the hysteresis loop is denoted by arrows.	20
7	Typical virtual cathode limit cycles in the classical short-circuited one-dimensional diode with an injection energy of 51 keV. a) $\alpha = 2.5$, b) $\alpha = 2.0$, c) $\alpha = 1.4$. The motion in a) is clockwise and in c) is counterclockwise. $\lambda = 1.0 c/\omega_p$.	21
8	Successive snapshots of electron beam momentum space and corresponding potential shape in the diode for $\alpha = 2.0$, $\lambda = 1.0 c/\omega_p$. The time between frames is $.5 \omega_p^{-1}$. The initial beam kinetic energy is 51 keV.	24
9	Electric field at the injection plane versus current, α , for $I=0$. The plot depicts the normal C-flow (stable) and C-overlap (unstable) solutions. The oscillating virtual cathode (stable) solution is also shown. Regions I and II define the domains of attraction of the normal-C and virtual cathode solutions near the SCL, $\alpha = 4/3$.	29

LIST OF ILLUSTRATIONS (Continued)

<u>Figure</u>		<u>Page</u>
10	Curves of scaled electric field at the injection plane, \tilde{E} , versus scaled current, A , for various values of charge neutralization, I . The curves represent slices through a 3-dimensional surface. The S and U indicate stable and unstable branches for the $I=1$ slice.	32
11	Anticipated optimal operating ranges for various sources of high power electromagnetic radiation. Several experimental points are included.	41
12	Variation of virtual cathode distance, ξ , from the one-dimensional diode center versus the difference between the injected current, δ_0 , and the current needed for bifurcation, δ_B , in units of the Child-Langmuir value. δ_B is assumed to have a value of 4 from the classical analysis.	44
13	CCUBE diagnostic of charge density, ρ_b , and potential, ϕ , as a function of a longitudinal distance, z , for an electron beam in a two-dimensional drift space with an imposed large axial magnetic field. ρ_b is normalized to its value at injection. The value of $(\gamma_0 - 1)$ is 4. Note that the minimum charge density and potential are separated in z .	46
14	Net current amplitude and spectrum for a probe placed between the anode and virtual cathode. $\gamma_0 = 5$ and $v_0 = 3 v_g$.	47
15	B_θ and E_z field probe histories and frequency spectrum for a simulation with $\gamma_0 = 5$, $v_0 = 3.7$ and $B_z = 0$. Field units are MeV/cm for a beam density of 10^{12} .	48
16	Average microwave frequency dependence on the square root of triode voltage (after Mahaffey, et. al.).	50
17	Fabrication drawing of the VIRCATOR vacuum vessel. All flanges are Conflat type to accept standard feedthrough hardware.	58
18	Sketch of the beam target assembly. The anode, annular limiter, and microwave entrance port are operated at ground potential, and the cathode is operated at negative high voltage.	61
19	Schematic of the pulse power circuit which drives the magnetic field coil.	65
20	Schematic of the lumped element Blumlein pulse-forming line. Initially 10 stages will be used to give a pulse length of 600 nanoseconds.	67
21	Schematic of the Blumlein charging and trigger circuit which drive the electron beam.	69

ABSTRACT

The theory of virtual cathode oscillation and a detailed experimental design of a millimeter wave virtual cathode oscillator (VIRCATOR) are presented. It is found that second order analytical approximations give an accurate value for the space-charge limiting current of an electron beam in cylindrical geometry. The same Green's function approach could be used on other geometries as well. Exceeding the space-charge limiting current is the necessary condition for virtual electrode formation. However, it does not explain the nature of the space-charge limit instability. The oscillatory stable state of the virtual cathode is found to originate at the bifurcation point of several stable and unstable electron beam states. An analysis of the nonlinear growth rate of the instability is derived.

The virtual cathode is in effect a relaxation oscillator. The advantage of the vircator over a reflex klystron is that the virtual cathode moves opposite to the electron beam propagation direction during the bunching phase resulting in enhanced electron densities unobtainable otherwise. The periodic time-dependent nature of the bunching results in efficient microwave generation. Experimental efficiencies of 12% and theoretical efficiencies of 20% have been obtained. The microwave frequency scales as the relativistic beam plasma frequency. This can be adjusted via an externally applied axial magnetic field. The result is an oscillator which is frequency agile over an order of magnitude without externally changing the physical configuration. Output powers of from kilowatts to gigawatts are obtainable based on the power source. Experimental results are reviewed and explained. The rationale for using a foilless diode as the electron beam source is given.

A detailed mechanical and electrical design is described. It entails placing the vircator in a high vacuum vessel with flexibility for further

development. The electrical power is pulse formed using a lumped artificial Blumlein line. The axial magnetic field is critically damped for component safety and circuit design simplicity. The beam source is a foilless diode with an annular limiter for collimation and prevention of electrons reflexing into the diode. A W-band (75-110 GHz) microwave grating spectrometer has been designed and constructed for diagnosis of the electromagnetic wave signal. The vircator design goal is 1 Megawatt at 100 GHz.

I. INTRODUCTION

Since the discovery of the Child-Langmuir relation^{1,2} it has been known that exceeding the limiting current of a diode leads to the development of a virtual cathode. Subsequently, numerous papers were written on experiments and theory relating to space charge limited flows. Reference 3 provides an excellent background and bibliography. More recently, the exact steady state solutions for electron beams in one-dimensional relativistic diodes⁴ and bounded drift spaces⁵ were derived. It is easily seen that for sufficiently large currents there exist two steady states for an electron beam, only one of which is stable.⁶ At the space-charge limit (SCL) these two states coalesce and above the SCL they disappear.⁷ As current is increased past the SCL, the beam develops a jump instability and relaxes into an oscillating state.

In the early 1960's, computer models were developed which quantitatively depicted the nonlinear oscillatory nature of the virtual cathode.⁸⁻¹⁰ These were one-dimensional, non-relativistic, electrostatic, multiple sheet models. References 8 and 9 qualitatively pointed out many interesting dependencies of the oscillation frequency and potential minimum position on injected current, thermal spread and circuit resistance. Reference 10 presents computer experiments with one and two species.

The phenomenon of virtual cathode formation in intense relativistic electron beams figures prominently in a number of high interest research areas. Devices used to produce high current ion beams for inertial confinement fusion--pinch reflex diode^{11,12} and reflex triodes^{13,14}-- depend on the virtual cathode to inhibit electron transport and use its potential well to accelerate ions. The recent concept of the spherical electron-to-ion converter¹⁵ requires a virtual cathode.

The virtual cathode plays a dominant role in areas other than production of light ion beams for fusion. It is attributed with the main role in collective ion acceleration in neutral gas.^{16,17} Control of virtual cathode motion is the mechanism for acceleration in the Ionization Front Accelerator.^{18,19} It is also the acceleration method in two concepts for collective effect accelerators.^{20,21} A final application is the use of virtual cathode oscillations to produce high power, short wavelength microwaves.²²⁻²⁵ Experiments using reflex triodes have already been produced 1.4 GW of power with 12% beam-to-RF efficiency.²⁶ It is this latter application which will be considered in this report.

The report is organized as follows. Section II provides an in-depth review of the analytical approach to determining the space-charge limiting current. It is shown by comparison with particle-in-cell simulations that this value can be predicted quite accurately. Section III analyzes the nature and nonlinear growth rate of the space-charge limit instability which leads to the formation of a virtual cathode. In Section IV the basic considerations in the application of the virtual cathode for generating coherent microwaves is presented. Finally, Section V gives a detailed design, both mechanical and electrical, of the millimeter wave vircator being built for this project.

II. THE SPACE-CHARGE LIMITING CURRENT

A. Theory

The concept of limiting current can be visualized in the following over-simplified physical picture. As particles from the electron beam (see Figure 1) enter the drift tube, the charge which they carry creates a potential barrier against further transmission of current. If the injected current is greater than the limiting current, the potential energy, $e\phi$, will exceed the kinetic energy of the beam $(\gamma_0 - 1)mc^2$, where

e = electronic charge

ϕ = electrostatic potential ≤ 0

γ = relativistic factor $(1 - \beta^2)^{-1/2}$

γ_0 = value of γ at injection

β = v/c

v = electron velocity

m = electron rest mass

At that position the barrier is large enough to stop the current and cause reflection of beam electrons. Thus, the deep potential well is called a virtual cathode. Note, however, that since the amplitude of the well fluctuates in time and space, the beam is never completely cut off by the virtual cathode.

The general space-charge limiting current problem does not lend itself to analytical solution. Instead theoretical work on the subject has attempted to solve for limiting currents, which develop in REBs, in the strictly electrostatic case. The solutions derived are only valid for beams in steady state equilibrium, i.e., $I_0 < I_L$. Also, the derivations depend on the following assumptions:

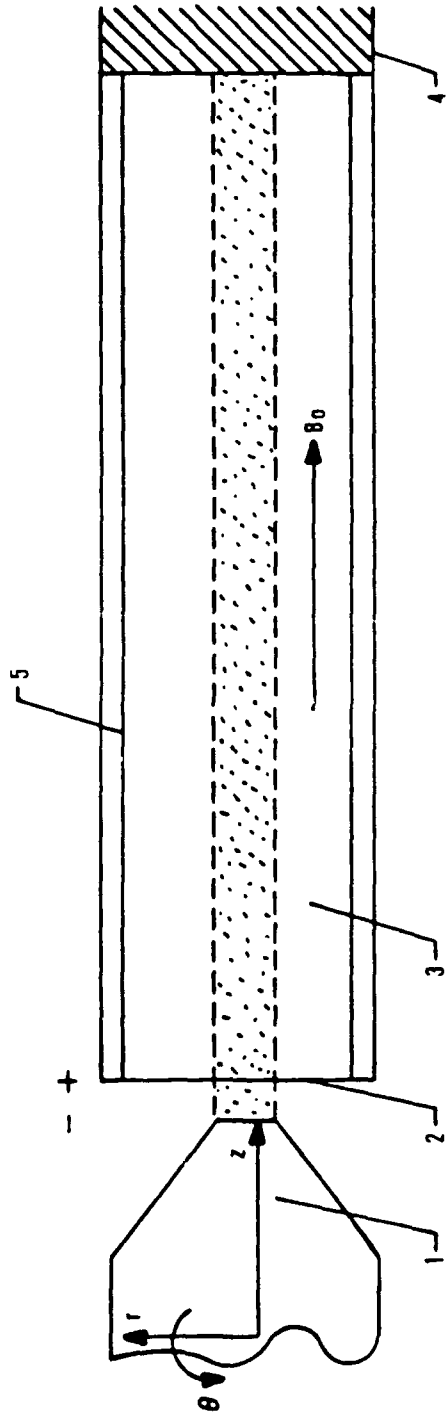


Figure 1. Schematic of a relativistic electron beam (REB): (1) cathode; (2) anode; (3) drift space; (4) collector; (5) return current conductor. The principal coordinate axes z , r , and θ are shown.

1. The electron beam is a cold plasma, $T_e = 0$. It implies the electrons are collisionless, and it allows one to neglect the ∇P_e and viscosity terms in the momentum transfer equation. Here, T_e is the electron temperature and P_e the electron pressure.

2. The electron beam is axially homogeneous and infinite. In real terms the infinite beam assumption implies $L \gg R$, where L is the drift tube length, and R is the drift tube radius. This allows the beam to reach a steady state far enough downstream from the injection plane to make the equilibrium beam density, n_b^0 , velocity, v^0 , and electric field, E^0 independent of z .

3. The equilibrium radial density and velocity profiles are azimuthally symmetric about the magnetic axis. In conjunction with paragraph 2 this means that n_b^0 , v^0 and E^0 are functions only of the radial distance, r .

4. The electron particle density and kinetic energy are independent of r at the anode plane. Therefore, the beam is uniform in space and monoenergetic at injection into the drift tube--anode foil scattering is neglected.

5. The externally imposed longitudinal magnetic field, \vec{B}_0 , is effectively infinite. If this assumption is not made, the current-induced equilibrium self-magnetic fields would play a major role in determining the equilibrium radial profile of the beam. Since \vec{B}_0 is taken as infinite, the electrons are guided and contained by it, and the self-fields can be treated as perturbations. Another way of expressing this assumption is to state that the Larmor radius of an electron in the \vec{B}_0 field must be much less than the beam radius, $r_L \ll r_b$.

Since assumptions 1 through 5 reduce the problem to the electrostatic case, solving Poisson's equation will give the desired result. Using this approach several researchers have derived expressions for the space-charge limited current of electron beams in vacuum and in charge neutral plasmas. Excellent reviews have been written.^{27,28} The most widely cited results are those of Bogdankevich and Rukhadze.²⁷ Using the conservation of energy and momentum they are able to write Poisson's equation for a cylindrically symmetric electron beam as

$$\frac{1}{r} \frac{\partial}{\partial r} \left(r \frac{\partial \phi}{\partial r} \right) = \begin{cases} -\frac{4\pi j}{c} \left[1 - \left(1 - \frac{e\phi}{mc^2} \right)^{-2} \right]^{-1/2} & 0 < r \leq r_0 \\ 0 & r_0 < r \leq R \end{cases}$$

with appropriate boundary conditions. Here, j is the current density. The radial cross section of the beam is given in Figure 2a, where R is the drift tube radius, and r_0 is the radius of the axially centered beam.

Equation (1) is a nonlinear differential equation. The approach taken in Reference 27 is to obtain solutions by making certain analytical approximations. These approximations are related to beam energy at injection (the nonrelativistic, $\gamma \approx 1$, or ultrarelativistic, $\gamma \gg 1$, limits) and beam geometry (the pencil beam, $\ln(R/r_0) \gg 1$, or fat beam, $\ln(R/r_0) \ll 1$ limits). The result is a series of first order analytical approximations which are restricted in validity to narrow regimes. Indeed, the most often used relation is an interpolation formula which utilizes the uniform density approximation. It neglects the radial variations in ϕ , γ , and number density, n . This equation consistently underestimates the true value of limiting current.

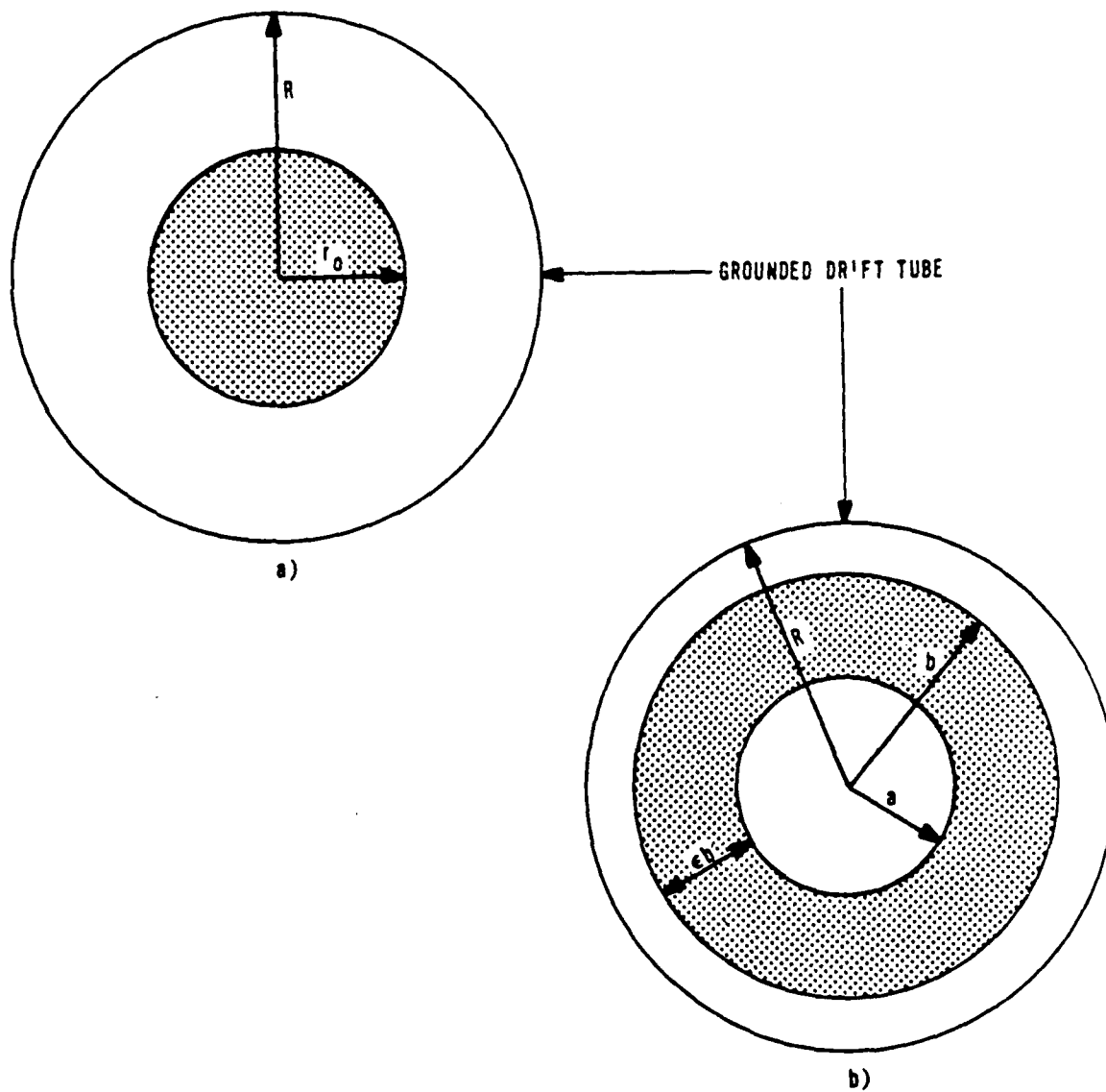


Figure 2. Radial cross section of two electron beams.
 (a) Solid beam where r_0 is the beam radius and R is the drift tube radius.
 (b) Annular beam where a is the inner radius, b the outer radius, R the drift tube radius and
 $\epsilon = \frac{b-a}{b}$.

The work of Genoni and Proctor²⁹ produces a more accurate, less restricted relation for space-charge limiting current. In particular, it is a second order analytical expression which takes into account the radial dependence of γ , ϕ , and n . Also, the beam is neither confined to the ultrarelativistic limit, nor is the beam geometry valid in only certain regimes. The general electron beam radial configuration is given in Figure 2b. As seen from the figure, R is the drift tube radius, a and b are the inner and outer beam radii, respectively, and $\epsilon = \frac{b-a}{b}$.

Their derivation also begins with conservation of energy and momentum, so that Poisson's equation for a cylindrically symmetric beam takes the form

$$\frac{1}{r} \frac{d}{dr} \left[r \frac{d\gamma(r)}{dr} \right] = \begin{cases} \frac{4\nu[(b/R)^2 - (a/R)^2]}{\beta(r)} & a \leq r \leq b \\ 0 & \text{elsewhere} \end{cases} \quad (2)$$

subject to the boundary conditions

$$\gamma(R) = \gamma_0 \qquad \gamma(0) \geq 1 \text{ and finite} \quad (3)$$

where $\nu = Ie/mc^3$ is dimensionless current independent of r and z . This is a nonlinear differential equation, as expected, showing the radial dependence of γ . By choosing an appropriate Green's function one can express equations (2) and (3) as an integral equation and obtain a numerical solution. More importantly, by assuming a uniform density radial profile of γ inside the beam as a zeroth order guess, one can iterate on the integral equation to obtain a second order analytical approximation to the current. Thus, not only can the limiting current be found by determining the value of γ which maximizes the current, but also the current in the drift tube for any value of γ and r can be evaluated. Using this approach an equivalent integral equation, valid for $a \leq r \leq b$, is

$$\gamma(r) = \gamma_0 - \frac{4v}{b^2 - a^2} \left\{ \ln \frac{R}{r} \int_a^r \frac{x}{\beta(x)} dx + \int_r^b \frac{x}{\beta(x)} \ln \frac{R}{r} dx \right\} \quad (4)$$

A first approximation $\gamma(r) = \gamma^I(r)$ is obtained by putting $\beta = K$ (a constant) in the integrals of equation (4). If K is fixed by requiring $\gamma^I(a) = (1 - K^2)^{-1/2}$, one obtains the following approximation to the limiting current:

$$v_L \approx v_L^{BR} \equiv \frac{(\gamma_0^{2/3} - 1)^{3/2}}{1 - f(\epsilon) + 2 \ln R/b} \quad (5)$$

where

$$f(\epsilon) = \frac{(1 - \epsilon)^2}{1 - \epsilon/2} \left| \frac{\ln(1 - \epsilon)}{\epsilon} \right| \quad (6)$$

Equation (5), which appears in a paper by Miller and Straw³⁰, is the logical generalization to annular beams of the widely used Bogdankevich-Rukhadze²⁷ interpolation formula for solid beams, to which it reduces in the limit $\epsilon \rightarrow 1$. A second approximation, $\gamma^{II}(r)$, is obtained by repeating this procedure using $\beta = [1 - (\gamma^I)^{-2}]^{1/2}$ in the integrals of equation (4). In the special case of a solid beam ($a = 0$), the integrals can be evaluated in closed form, but for the general case of an annular beam they must be done numerically. Genoni and Proctor²⁹ have obtained useful analytical approximations to $\gamma^{II}(r)$ for annular beams by doing the second iteration with $\beta = (1 - \Gamma^{-2})^{1/2}$ where $\Gamma(r)$ is a quadratic fit to $\gamma^I(r)$ which yields the exact $\gamma^{II}(r)$ in the solid beam limit. A particular choice of K then yields a definite relation between v and $\gamma_a \equiv \gamma(a)$. The simplest of these that gives good agreement with numerical results is evidently

$$v = \frac{(\gamma_0 - \gamma_a)^2}{(\Gamma_b^2 - K)^{1/2} - (\gamma_a^2 - 1)^{1/2}} \frac{1 - g}{(1 - f + 2 \ln R/b)^2} \quad (7)$$

in which

$$\Gamma_b = \gamma_a + (\gamma_0 - \gamma_a) \frac{1 - g}{1 - f + 2 \ln R/b} \quad (8)$$

and

$$g(\epsilon) = \frac{8(1 - \epsilon)^2}{\epsilon(4 - 3\epsilon)} \ln \frac{1 - \epsilon/2}{1 - \epsilon} \quad (9)$$

In the limit $\epsilon \rightarrow 1$, both g and f tend to zero, and equation (7) reduces to a formula (equation 14) obtained by Thompson and Sloan (Ref. 8) in their analysis of solid beams. It should be noted that different quadratic fits, while producing more complicated analytical expressions, produce more accurate results.²⁹

B. Simulation

The space-charge flow simulations were carried out using a two-dimensional particle-in-cell plasma simulation code, CCUBE, which is fully relativistic and electromagnetic.^{32,33} CCUBE (Version One) solves self-consistently for the time-dependent trajectories of tens of thousands of plasma particles over thousands of plasma periods. The critical portion of the code consists of a leap frog procedure. At each time step, the charge and current associated with the particles are interpolated bilinearly onto a spatial mesh. The quantities then serve as source terms in Maxwell's equations for determining the electromagnetic scalar and vector potentials on the mesh. Finally, the potentials are interpolated back to the particle positions. The basic coordinate system is cylindrical with azimuthal symmetry assumed. A uniform axially directed magnetic field can be imposed to insure beam equilibrium.

All variables are expressed in dimensionless terms. In particular, the depth of the potential well formed by the electronic space-charge is given by ϕ , where

$$\phi(r) = \frac{e\Phi(r)}{mc^2} = \gamma(r) - \gamma_0 \leq 0 \quad (10)$$

The five components in configuration-momentum space are $X1 = z \omega_p^0/c$, $X2 = r \omega_p^0/c$, $V1 = \gamma \beta_z$, $V2 = \gamma \beta_r$, $V3 = \gamma \beta_\theta$ where β_z, β_r , and β_θ are the components of β in the z , r , and θ directions, respectively. $\omega_p^0 = (4\pi n_b^{inj} e^2/m)^{1/2}$ is the electron plasma frequency arising from the beam density at injection, n_b^{inj} .

In these simulations the code is made to model the injection of cold, monoenergetic, relativistic electrons with uniform density into a long, evacuated, equipotential, cylindrical drift tube along an effectively infinite magnetic guide field in order to comply with the assumptions of the previous section. This is accomplished in the following manner.

1. A cold beam is obtained by setting the electron thermal velocity components equal to zero.
2. Miller and Straw³⁴ provide a criterion for neglecting the presence of end plates and effectively having $L \gg R$.

$$L/R \geq 2.58 (b/R)^{0.133} \quad (11)$$

For the annular beam simulations this yields $L/R \geq 2.50$, whereas the worst case simulation is $L/R = 9.84$. In addition, two runs were made with the downstream axial boundary grounded. The presence of end plates did not affect the results.

3. Azimuthal symmetry is assured by the nature of the code.
4. The code injection can be made to neglect anode foil scattering, so that the particles are monoenergetic and spatially uniform at injection.
5. Thode, et al.³⁵, give a numerical relation to insure that the imposed magnetic field is effectively infinite. It is $\omega_c/\omega_p^0 \geq 5$ where ω_c is the beam cyclotron frequency defined as eB_0/mc . This is met by running the code's dimensionless, external, magnetic field as

$$B_0 = \omega_c / \omega_p^0 = 8.0 \quad (12)$$

The number of cells in the X1 and X2 direction were 190 and 37, respectively. The X1 length was held constant at 50.0 units giving $\Delta X1 = 0.263$ per cell. The X2 radius varied from 2.89 to 5.0 depending on the value of injected current. The boundary conditions for the electrons are reflection at the axis and absorption on both the radial and axial surfaces. Potentials are set to zero at the upstream axial and outer radial boundaries in order to represent metal surfaces. At the downstream axial boundary, however, the normal derivatives of the potentials are set to zero in order to mock up an infinitely long cylinder.

In the next section, the value of γ_a from the simulation calculation is compared, for a given value of ν , with that given by equation (7), as well as with a numerical solution obtained by iterating on equation (4) with $r = a$.²⁹

C. Results

Several CCUBE runs were made using $\gamma_0 = 5$ and varying values of ν in order to determine the maximum value of $|\phi|$. This occurred consistently at the radial value $r = a$. Therefore, $|\phi|$ maximizes for $\phi(a) \equiv \phi_a$. The characteristics of the simulation runs are given in Table 1. The last column in Table 1 refers to whether the downstream axial boundary was grounded or open. Such a condition enabled us to check whether or not end plate effects were entering the problem. As seen in Table 1 no effects were noted. The percent error was derived on the basis of the code's management of conservation of energy, which is denoted by a net energy diagnostic. Since net energy continuously increases due to roundoff and truncation errors, the percent error will increase as a function of computer run time. The percent errors given in Table 1 were taken after the run reached a steady state, as denoted by total energy and $|\phi|$ reaching a constant, or a virtual cathode was formed. The latter case was true in runs 3 and 8.

This can be observed in the table, since $|\phi_a| > (\gamma_0 - 1)$. Thus, the space-charge limiting current lies between $\nu = 1.175$ and 1.293 for the solid beam case and $\nu = 2.846$ and 3.034 for the annular beam case.

TABLE 1
CHARACTERISTICS OF SIMULATION RUNS

Run	ν	$ \phi_a $	Error (%)	a/R	b/R	$L(c/\omega_p^0)$	$R(c/\omega_p^0)$	Downstream Axial Boundary
1	1.175	3.07	1.5	0	0.5	50.0	4.38	0
2	1.175	3.06	1.2	0	0.5	50.0	4.38	G
3	1.293	4.20	2.5	0	0.5	50.0	4.60	0
4	0.982	1.01	0.74	0.4	0.8	50.0	2.89	0
5	1.957	2.05	1.1	0.4	0.8	50.0	4.08	0
6	2.846	3.18	1.2	0.4	0.8	50.0	4.92	0
7	2.846	3.18	1.1	0.4	0.8	50.0	4.92	G
8	3.034	4.25	3.1	0.4	0.8	50.0	5.08	0

A comparison is made between the numerical, analytical and simulation models in Table 2. All three methods produce consistent values of γ_a for given values of sublimiting injected current. Table 2 lists the values given by the three methods, where

$$\gamma_a = \gamma_0 - |\phi_a| \quad (13)$$

is used to define γ_a for the simulations. Note that if a virtual cathode is formed, $|\phi_a| > (\gamma_0 - 1)$, γ_a as defined by equation (13) does not have a physical meaning. Rather, it is simply a mathematical relation between γ_0 and $|\phi_a|$.

TABLE 2
COMPARISON OF MODELS

ν	γ_a Numerical	γ_a Analytical	γ_a Simulation	Beam Type
1.175	1.893	1.93	1.93	Solid
1.293	Virtual Cathode	Virtual Cathode	Virtual Cathode	Solid
0.982	4.004	4.00	3.99	Annular
1.957	2.976	2.98	2.95	Annular
2.846	1.867	1.92	1.82	Annular
3.034	Virtual Cathode	Virtual Cathode	Virtual Cathode	Annular

A more important comparison can be made between the values for space-charge limiting current, ν_L , derived from the numerical, analytical, and simulation models and that produced by the widely used Bogdankevich-Rukhadze interpolation formula, equation (5). This is done in Table 3. Equation (5) predicts values for ν_L which are significantly lower than those of equation (4) and (7). However, the analytical results differ from the figures given by the integral equation by roughly 3 percent. ν_L is obtained from equation (4) by determining numerically the largest value of ν for which a solution exists. The limiting current for equation (7) is derived from the value of γ_a which maximizes ν .

TABLE 3
LIMITING CURRENT COMPARISON

Beam Type	ν_L Numerical	ν_L Analytical	ν_L Simulation	ν_L B-R
Solid	1.27	1.31	1.175 - 1.293	1.118
Annular	3.03	3.12	2.846 - 3.034	2.712

The discrepancy in the limiting value of v between the Bogdankevich-Rukhadze and Genoni-Proctor formulations is due to the error involved in assuming the uniform density approximation. Figure 3 is a plot of the relation between v and γ_a in the uniform density approximation and in a second order analytical expression using a better quadratic fit than equation (7). The simulation points are added. It is clear that the uniform density approximation underestimates the value of v for all values of γ_a . Finally, Figure 4 plots $\gamma(r) - 1$ versus r . It shows the dependence of beam kinetic energy on r for the annular beam modeled. The successively more energetic lines of dots correspond to the more recent injections of charge through anode. As expected, the minimum kinetic energy occurs at the inner beam edge, and the maximum occurs on the outer edge. The uniform density approximation neglects this dependence.

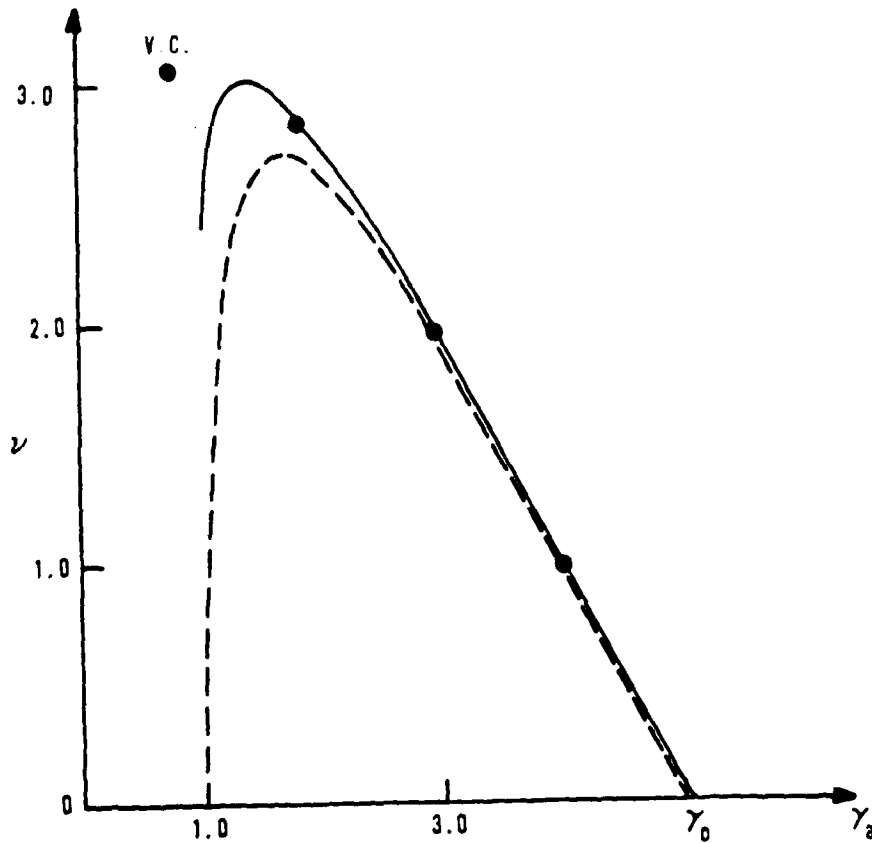


Figure 3. Plot of ν versus γ_a for $\gamma_0 = 5$, $a/R = 0.4$, $b/R = 0.8$. The dashed line represents the uniform density approximation. The solid line results from an approximate second order analytical relation. The points correspond to simulation results. (N.B. γ_a for the point labeled v.c. (virtual cathode) has no physical meaning. It is defined in terms of equation (13)).

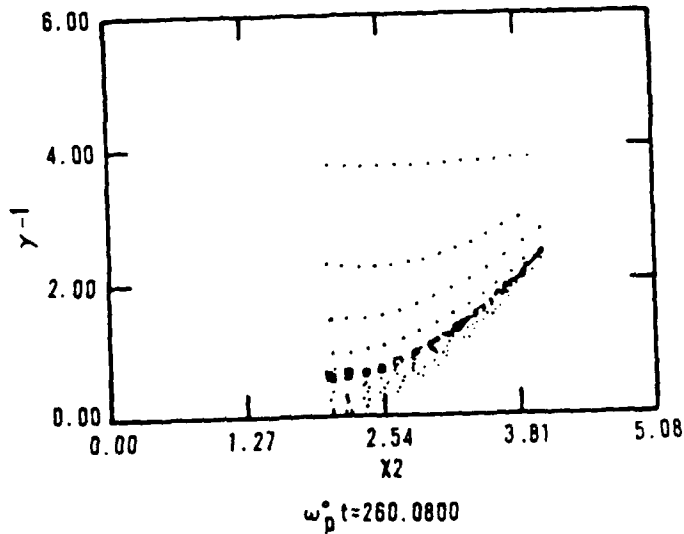


Figure 4. A CCUBE diagnostic of particle kinetic energy versus r for the annular beam showing the radial dependence of γ .

III. THE SPACE-CHARGE LIMIT INSTABILITY

We have visualized the space-charge limiting current as a point at which the electrostatic potential exceeds the kinetic energy of the beam. However, it is easily noted from Figure 3 that at the SCL the beam kinetic energy is approximately $\gamma_0^{1/3}mc^2$. Thus, although the onset of virtual cathode formation can be exactly predicted as the point at which the beam exceeds a critical current, the dynamics of its formation and subsequent oscillations are not well understood.

A small signal perturbations analysis can be performed just below the SCL which seems to predict instability above the limiting current value,^{6,9} however, it is not rigorous and in fact produces misleading results. Instead one can use multiple scaling perturbation techniques to study the time dependent behavior of a beam when the SCL is exceeded. We derive estimates for the nonlinear growth rate of the ensuing instability and show that even below the SCL the beam is unstable to sufficiently large perturbations. The method can be applied to a wide class of problems, but here we treat the short-circuited one-dimensional electrostatic diode depicted in Fig. 5 as the simplest model containing the appropriate physics. We show that, at least in one dimension, an arbitrarily heavy ion background does not alter the qualitative behavior of the beam, and present numerical results that exhibit virtual cathode oscillations for a neutral beam. Before starting this analysis, it is worthwhile to describe the results of numerical simulations to present a picture of time-dependent virtual cathode dynamics.

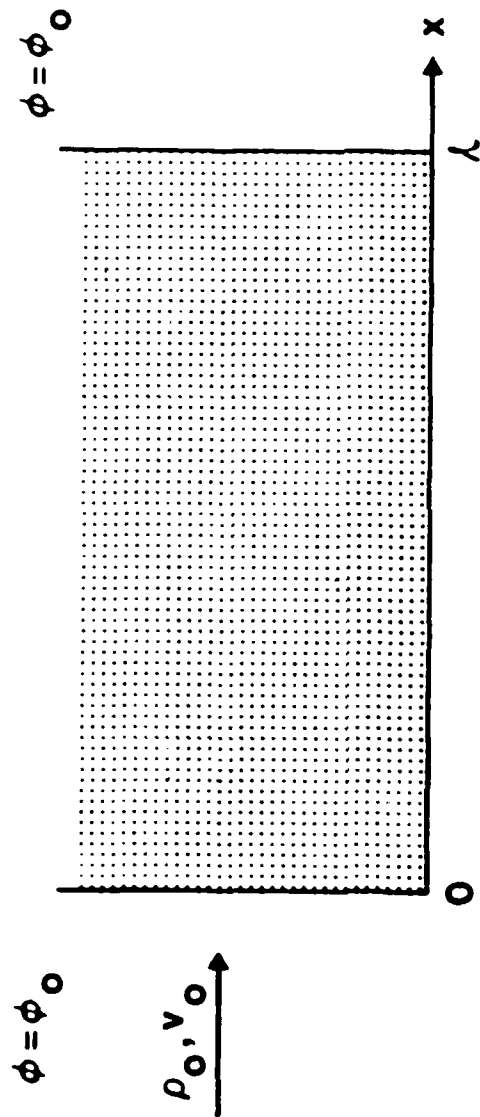


Figure 5. Schematic of the short-circuited one-dimensional electrostatic diode modelled in this study.

A. Physical Description of the Virtual Cathode

Simulations were carried out in conjunction with the theory presented in the next section using a two-dimensional, relativistic, electrostatic, particle-in-cell code. The code can solve self-consistently for the time dependent trajectories of tens of thousands of plasma particles over thousands of plasma periods. All variables are expressed in dimensionless terms. Therefore, length is in units of c/ω_p ; time is measured in units of ω_p^{-1} , and particle velocity is given by $v_i = \beta_i \gamma$ ($i = 1, 2, 3$), where ω_p is the initial electron plasma frequency.

In these simulations a monoenergetic 51 keV electron beam is injected into a Cartesian geometry. The left and right boundaries are grounded representing a planar short-circuited diode. Periodic boundary conditions in the transverse direction make configuration space effectively one-dimensional. In general, the simulation had 62 cells in the longitudinal direction modelling a length of $1.0 c/\omega_p$. The time step was $0.0125 \omega_p^{-1}$. Twenty particles were injected per cell.

A detailed discussion of the physical dynamics of the virtual cathode based on these numerical results is appropriate here. The usual graph of potential minimum, ϕ_m , in the diode versus electron beam current, α , is shown in Fig. 6. The parameter α will be discussed later. When α is increased above the space-charge limit, ϕ_m jumps from the stable normal-C branch to the oscillatory stable branch. The amplitude and position of ϕ_m while on the oscillatory branch describe a limit cycle, as expected for a relaxation oscillation which this represents. Typical limit cycles are depicted in Fig. 7. As α is increased further, ϕ_m , the oscillation frequency, and virtual cathode position within the diode asymptotically approach limiting values. If α is decreased, the oscillation amplitude, $\Delta\phi_m$, decreases and the position of ϕ_m moves toward the diode center.

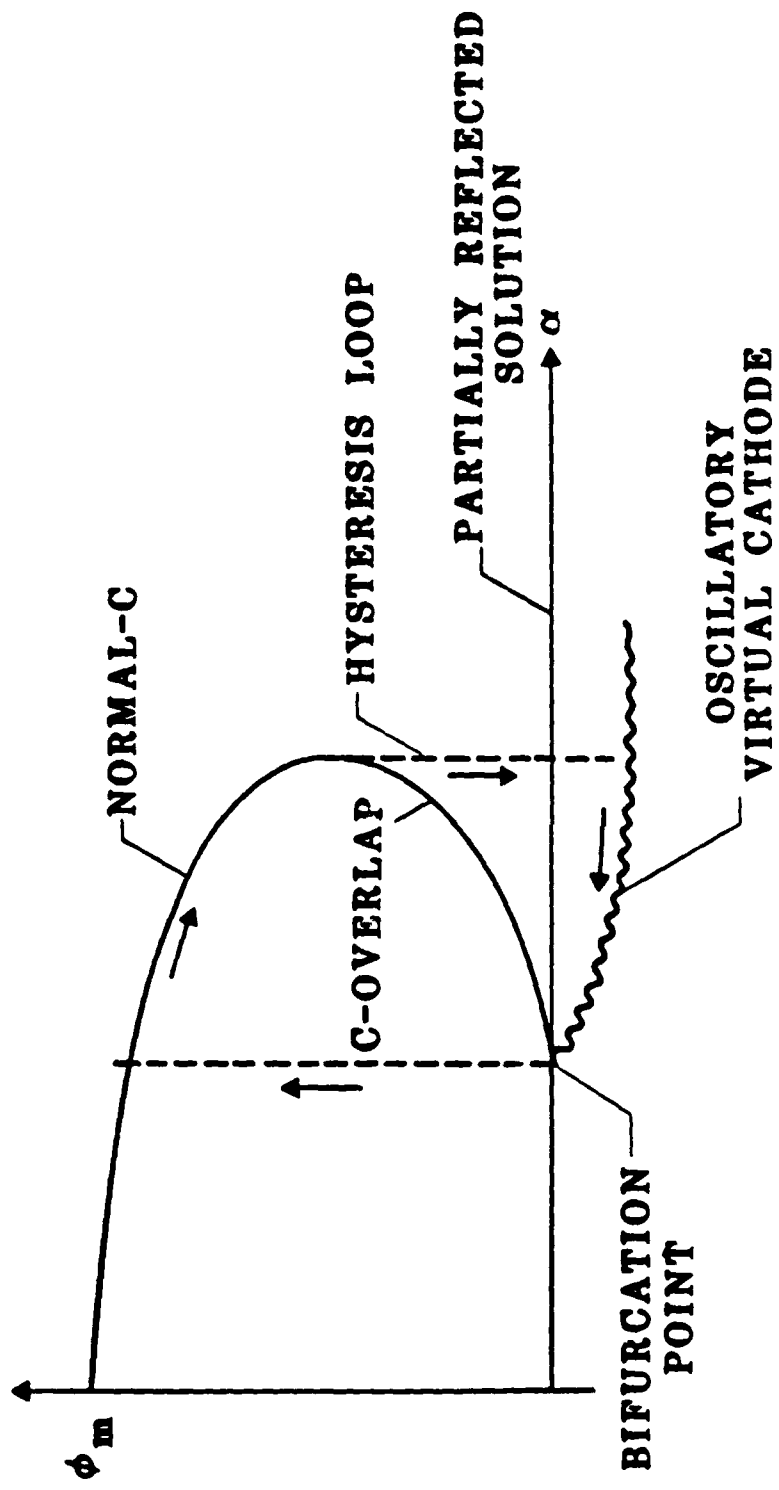


Figure 6. Electrostatic potential minimum as a function of current, α . The plot depicts the various possible solutions such as normal-C flow (stable), C-overlap (unstable), the partially reflected solution (unstable) and the oscillatory virtual cathode (stable). The motion around the hysteresis loop is denoted by arrows.

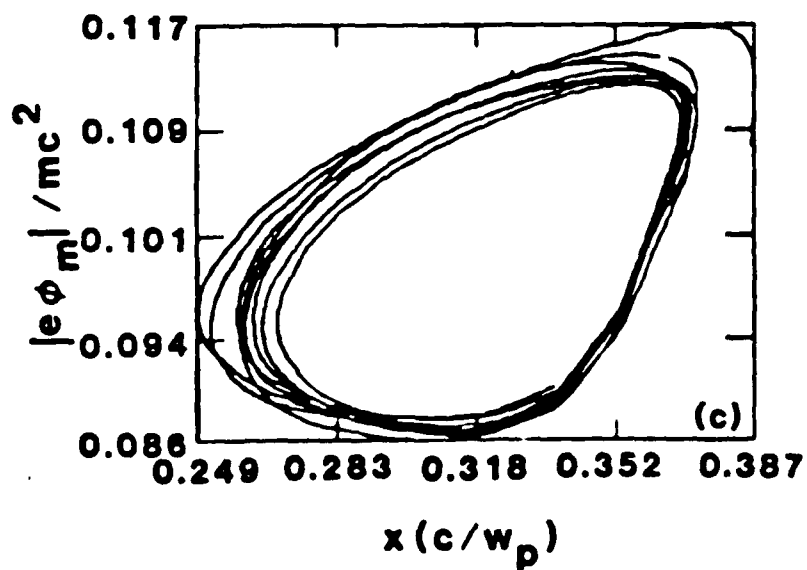
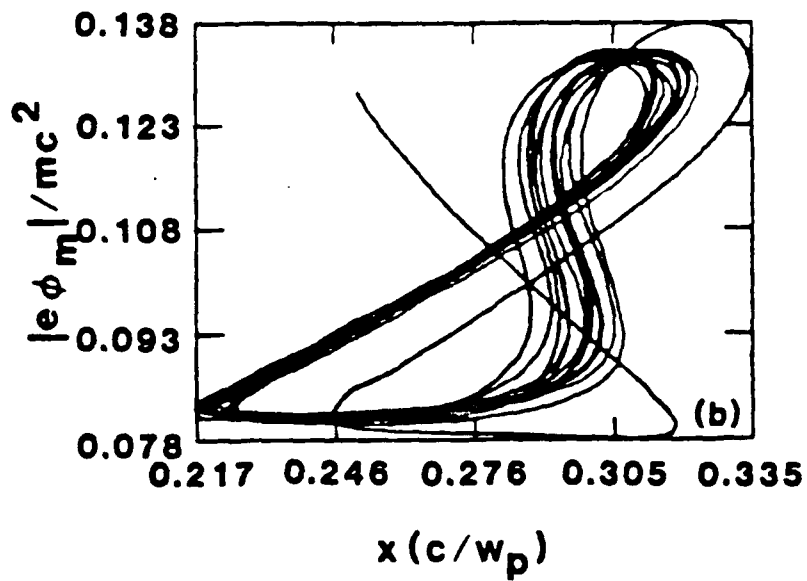
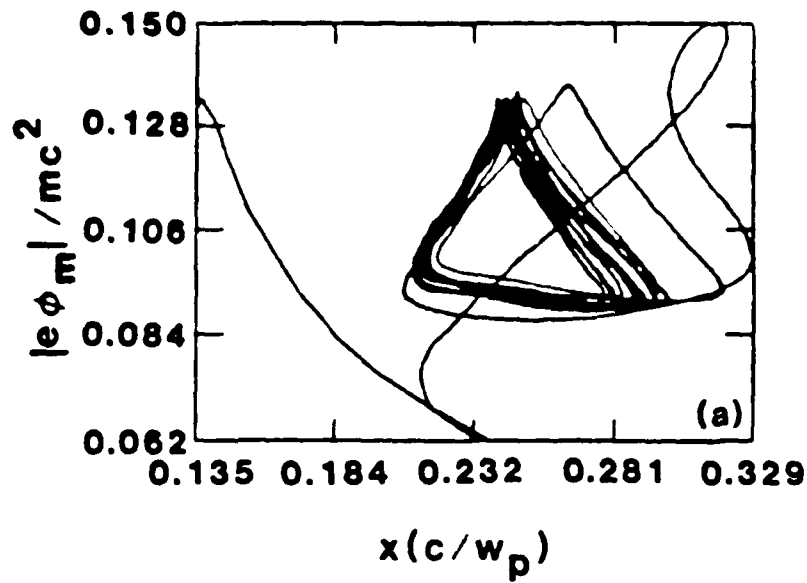


Figure 7. Typical virtual cathode limit cycles in the classical short-circuited one-dimensional diode with an injection energy of 51 keV. a) $\alpha = 2.5$, b) $\alpha = 2.0$, c) $\alpha = 1.4$. The motion in a) is clockwise and in c) is counterclockwise. $\ell = 1.0 c/w_p$.

The electron flow reverts to the equilibrium steady state when the perturbation due to the rate of change of diode current below the space-charge limit is sufficiently large. This normally occurs before the bifurcation point is reached. The entire process forms a hysteresis loop, which is depicted in Fig. 6.

The virtual cathode originates at the bifurcation point. This is the intersection of the oscillatory state with the C-overlap⁷ and partially reflected solution branches.⁵ The bifurcation point cannot be reached in the short-circuited diode. Of the three branches emanating from it two (the steady ones) are physically unstable while the oscillatory branch is numerically unstable at this point. This results because the limit cycle at the bifurcation point is infinitesimally small, so that simulation codes lose resolution before it can be reached. Loss of resolution creates a small amplitude, high frequency oscillation observed in this study and previously.⁹ This result is numerical, not physical.

This problem can be overcome, if we eliminate the hysteresis loop. Then the C-overlap branch disappears and we can get to the bifurcation point along the stable normal-C branch. This can be accomplished in several ways. The most appropriate in this study is to have a retarding potential difference across the diode equal to the injected electron kinetic-energy. Then the C-overlap solution vanishes and the bifurcation takes place at the space-charge limit, α_{SCL} . The oscillation can be described as a small perturbation on the beam rather than the radical change that results in the short-circuited diode when α_{SCL} is exceeded. This analysis indicates that the onset of virtual cathode formation occurs when the electron velocity in the steady state vanishes at some point inside the diode. For the short circuited diode this occurs at the diode center; for the biased diode it occurs at $x \leq \ell$. Because the oscillation is a small perturbation on the steady state fields in the biased diode, it is readily seen that the virtual cathode oscillation period at

onset is the electron transit time from the injection plane to the position where velocity vanishes.

Finally, consider the particle dynamics during the oscillation period for counterclockwise limit cycles ($\alpha \leq \alpha_{SCL}$) as in Fig. 7c. At the point where the virtual cathode position is a minimum and the potential well is starting to move to the right, its amplitude is too small to stop the electrons. When its motion is to the left it opposes the electron beam and causes particle bunching. Since the well is deeper, the stream velocity will vanish at some location and then become negative. Here, the second derivative of the velocity (d^2u/dx^2) is also negative. In this process the stream is continuously deformed to create a double valued negative velocity protrusion. The entire system is three valued (Fig. 8), as in a collisionless shock wave.³⁶ Here, the region of triple flow is not limited, as in usual collisionless shocks, by the presence of a transverse magnetic field,³⁷ but rather by the presence of the walls. Indeed, the reflected part detaches from the main beam and exits through the anode periodically, thus being responsible for the onset of oscillatory behavior in beam characteristics. As the potential minimum reaches the end of its left motion the two "lips" of the back reflected stream close. At this point no more electrons are reflected and the well moves to the right repeating the cycle.

For larger values of α the limit cycle is distorted into a figure 8 with one lobe having clockwise and the other counterclockwise motion (Fig. 7b). This transition continues until the motion is completely clockwise (Fig. 7a). It indicates a change in the particle bunching process and is related to the fraction of current which is reflected versus transmitted from the injected electron beam. In Figure 7a most of the beam is reflected whereas in Fig. 7c most electrons are transmitted.

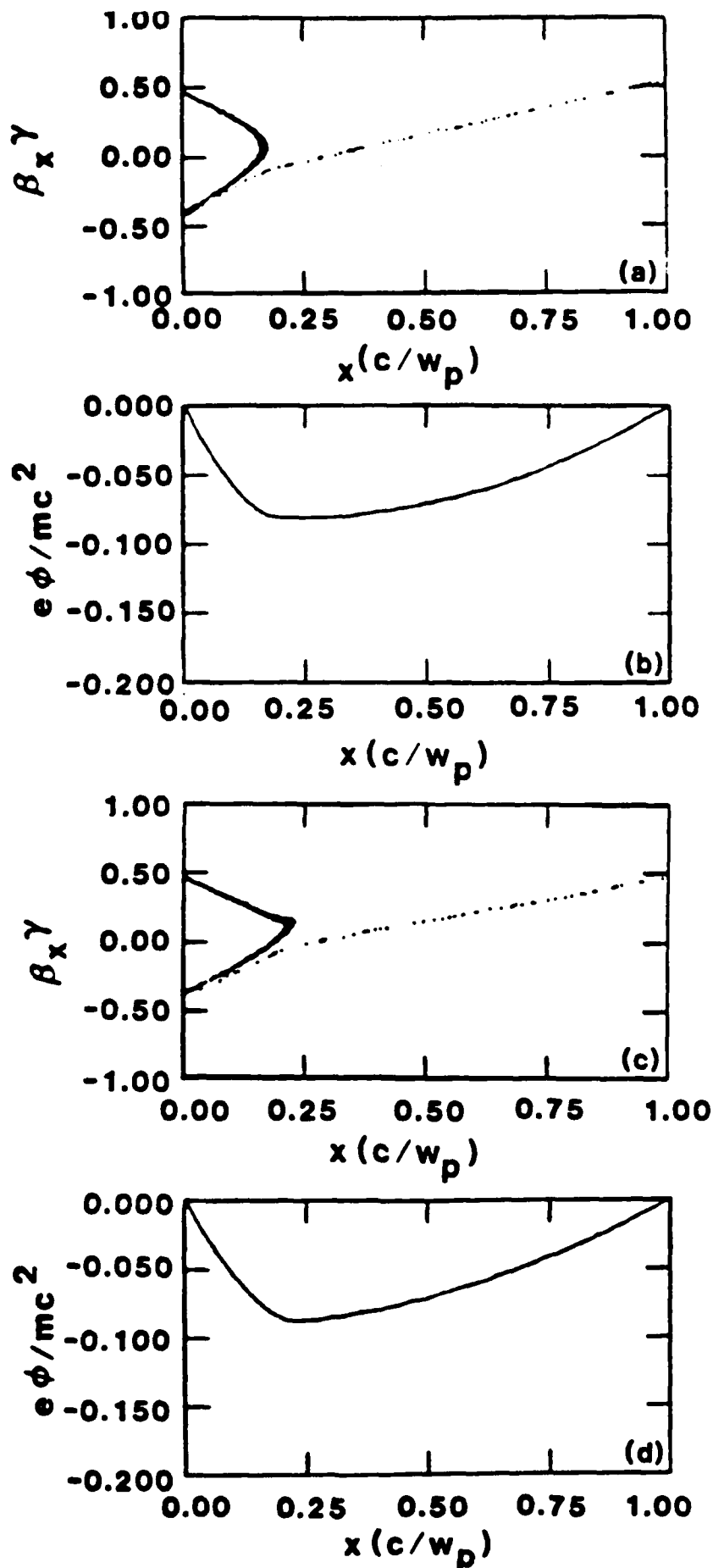


Figure 8. Successive snapshots of electron beam momentum space and corresponding potential shape in the diode for $\alpha = 2.0$, $\ell = 1.0$ c/w_p . The time between frames is $.5 \omega_p^{-1}$. The initial beam kinetic energy is 51 keV.

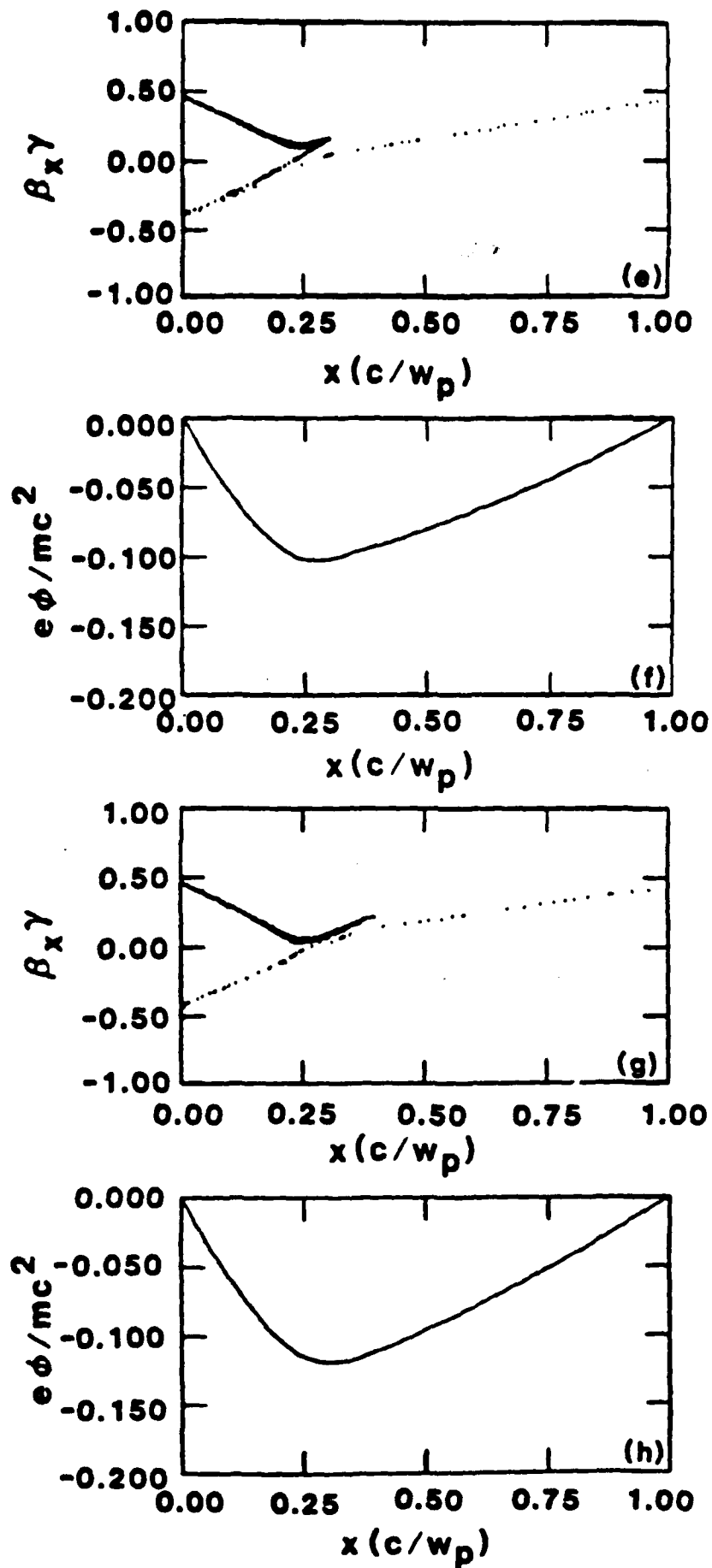


Figure 8. Concluded.

8. Theory

The one-dimensional motion of electrons in the diode is given by the equations of continuity, and momentum conservation for the electrons plus Poisson's equation. They are expressed here as

$$\rho_{\tilde{t}} + (\rho v)_{\tilde{x}} = 0 \quad (14a)$$

$$v_{\tilde{t}} + v v_{\tilde{x}} = -\frac{e}{m} \xi \quad (14b)$$

$$\epsilon_0 \xi_{\tilde{x}} = \rho + \rho_h \quad (14c)$$

where $0 \leq \tilde{x} \leq l$. The subscripts denote differentiation with respect to that variable. Electron and heavy ion charge density, electron velocity, electric field, time and position are indicated by ρ , ρ_h , v , ξ , \tilde{t} , and \tilde{x} , respectively. The appropriate boundary conditions are $v(0, \tilde{t}) = v_0$, $\rho(0, \tilde{t}) = \rho_0$ and $\int \xi d\tilde{x} = 0$. An ion component is placed in Poisson's equation in order to discuss two-specie space-charge flow. Conservation equations of mass and momentum for the heavy ions are not included, because it is assumed that their velocity does not change appreciably during their passage through the diode.

In order to simplify the mathematics, we introduce dimensionless equations for our model. They are

$$n_{\tilde{t}} + (nu)_{\tilde{x}} = 0 \quad (15a)$$

$$u_{\tilde{t}} + uu_{\tilde{x}} = -\alpha E \quad (15b)$$

$$E_{\tilde{x}} = \alpha(n + I) \quad (15c)$$

where $n = \rho/|\rho_0|$, $u = v/v_0$, $E = (e\epsilon_0/m|\rho_0|)^{1/2} \xi/v_0$, $t = v_0\bar{t}/\ell$, $\bar{x} = x/\ell$,
 $\alpha = (e|\rho_0|/\epsilon_0 m)^{1/2} \ell/v_0$ a dimensionless parameter related to current,
and I the ratio of heavy ion to electron charge densities, $I = \rho_h/|\rho_0|$.
Alternatively, α may be written as $\ell\omega_p/v_0$ where ω_p is the beam plasma
frequency. The boundary conditions for electrons become $u(0, t) = 1$,
 $n(0, t) = -1$, and $\int_0^1 E dx = 0$. For an ion beam $n(0, t) = 1$, otherwise the
following derivation is the same.

1. Unneutralized Beams

For an unneutralized beam, setting $I = 0$ and solving by the method of
characteristics^{38,39} we find

$$n^{-1} = -\frac{\alpha^2}{2} (t-s)^2 + \alpha E_0(s) (t-s) - 1 \quad (16)$$

where s is the entry time for the particle occupying position x at time t
and $E_0(s)$ is the electric field at $x = 0$. The particle trajectories are
found by utilizing equation 15a, from which it follows that

$$\left(\frac{\partial x}{\partial s}\right)_t = n^{-1}. \quad (17)$$

This yields

$$x = \frac{\alpha^2}{6} (t-s)^3 + \alpha \int_t^s E_0(s) (t-s) ds + (t-s) \quad (18)$$

Integration of the trajectory equation is hard for general time-dependent situations, because imposing the proper boundary conditions leads to a nonlinear integral equation for $E_0(t)$. However, several special cases can be solved exactly. The problem of injection into an empty diode can be integrated until the formation of a singularity in n , indicating the crossing of trajectories.³⁹ In this case the stream velocity becomes 3-valued and one must use a Vlasov equation description,⁴⁰ rather than system (15) that is derived assuming a single stream of monoenergetic particles. As described in the previous section this multistreaming is characteristic of the oscillatory state created when α exceeds its SCL value.

Using these equations we can derive a similar representation for Fig. 6 in terms of E_0 and α . For steady states, $E_0(t) = E_0$, a constant, we find

$$u = -n^{-1} = \frac{\alpha}{2} (t-s)^2 - \alpha E_0 (t-s) + 1 \quad (19a)$$

$$x = \frac{\alpha}{6} (t-s)^3 - \frac{\alpha}{2} E_0 (t-s)^2 + (t-s) \quad (19b)$$

Imposing the conditions $x = 1$, $u = 1$ at $t-s = t_0$, the particle transit time, we note that t_0 must satisfy

$$\frac{\alpha}{12} t_0^3 - t_0 + 1 = 0 \quad (20)$$

This equation has two positive solutions for $0 \leq \alpha \leq 4/3$, coalescing at $\alpha = 4/3$. The largest one, for $0 \leq \alpha < 2\sqrt{2/3}$ does not correspond to a real flow. In Fig. 9 we show $E_0 (= \alpha t_0/2)$ vs. α . This representation will be used in the discussion of nonlinear stability.

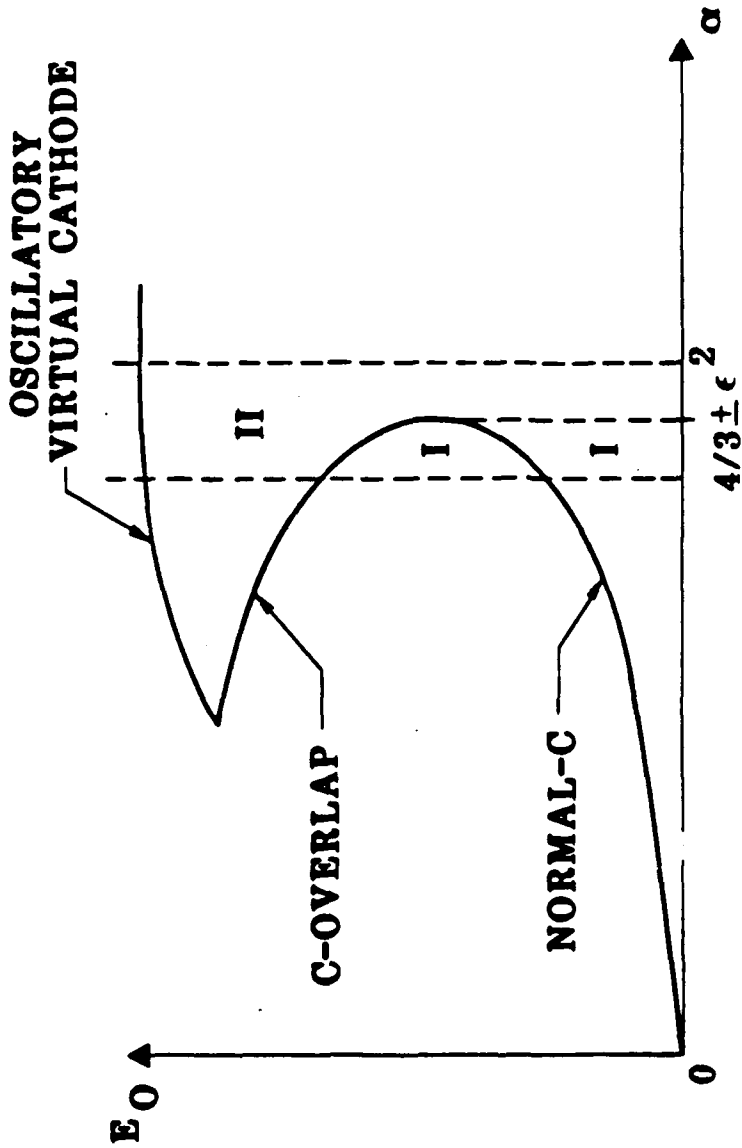


Figure 9. Electric field at the injection plane versus current, α , for $I=0$. The plot depicts the normal C-flow (stable) and C-overlap (unstable) solutions. The oscillating virtual cathode (stable) solution is also shown. Regions I and II define the domains of attraction of the normal-C and virtual cathode solutions near the SCL, $\alpha = 4/3$.

2. Neutralized Beams

The Pierce instability occurs when electron and ion space-charge flow is considered in finite geometries where there is no potential difference across the boundaries.⁴¹ The ions can be stationary or moving with respect to electrons. Charge neutrality is maintained at the injection plane. This instability may have ramifications for charged particle inertial confinement fusion because of its effect on neutralized beam propagation in the reactor.⁴² In this section we show that the Pierce instability is a special case of electron and ion space-charge flow. In general, two species flow has steady and oscillatory states analogous to one species space-charge flow.

The steady state behavior for the case of arbitrary I can be found in a manner similar to $I = 0$. Rewriting system (15) in characteristic coordinates we arrive at

$$\frac{d^2}{dt^2} \left(1 + \frac{I}{n}\right) + \alpha^2 I \left(1 + \frac{I}{n}\right) = 0 \quad (21)$$

For positive ions ($I > 0$) the solution of (21) after satisfying the boundary conditions is

$$1 + \frac{I}{n} = (1 + I) \cos \alpha \sqrt{I}(t-s) + E_0 \sqrt{I} \sin \alpha \sqrt{I}(t-s) \quad (22)$$

Imposing conditions $x = 1, u = 1$ at $t-s = t_0$, we find the system

$$1 = \frac{1}{I} t_0 - \left(\frac{1-I}{\alpha I^{3/2}}\right) \sin \alpha \sqrt{I} t_0 + \frac{E_0}{\alpha I} (\cos \alpha \sqrt{I} t_0 - 1) \quad (23a)$$

$$1 = \frac{1}{I} - \frac{1-I}{I} \cos \alpha \sqrt{I} t_0 - \frac{E_0}{I} \sin \alpha \sqrt{I} t_0 \quad (23b)$$

For $I = 1$, which implies charge neutralization, these equations reduce to the relations given in Reference 43 for the Pierce instability. However, by varying I the curves shown in Figure 10 are obtained. These are cuts at constant I through a three-dimensional contiguous surface. The space is defined by the axes $\bar{E} = E_0 I^{1/2}$, $A = \alpha I^{3/2}$ and I . The surface is 2π periodic in A with the vertical plane at $A = 2\pi$ being common for all values of I . For given A a linearized analysis establishes that the equilibria denoted by the curves are stable (unstable) for the lowest (highest) value of \bar{E} . At $I = 1$ exchange of stability takes place at odd multiples of π . For $I < 1$ exchange of stability occurs at the points where $dE_0/d\alpha \rightarrow \infty$.

It is evident from Fig. 10 that, for $I < 1$, there are no stable equilibrium solutions in the neighborhood of $A = \pi$. Therefore, one expects a virtual cathode to form when $I < 1$ and A adiabatically increases to π . We have found, by using numerical simulation, that in this case the beam settles to an oscillatory state, similar to the virtual cathode for unneutralized beams.⁴⁰ By slowly increasing I past the neutral beam value of 1 in our simulation, we have established that this oscillation persists. Indeed, finding this oscillatory state for $I > 1$ by other means would have been difficult, because the simulation would tend to follow the stable steady branch that is present for all values of current.

3. Nonlinear Stability Analysis

For $I < 1$, it is of interest to establish the properties of the beam instability at the SCL - generalized for $I \neq 0$ to mean the point where

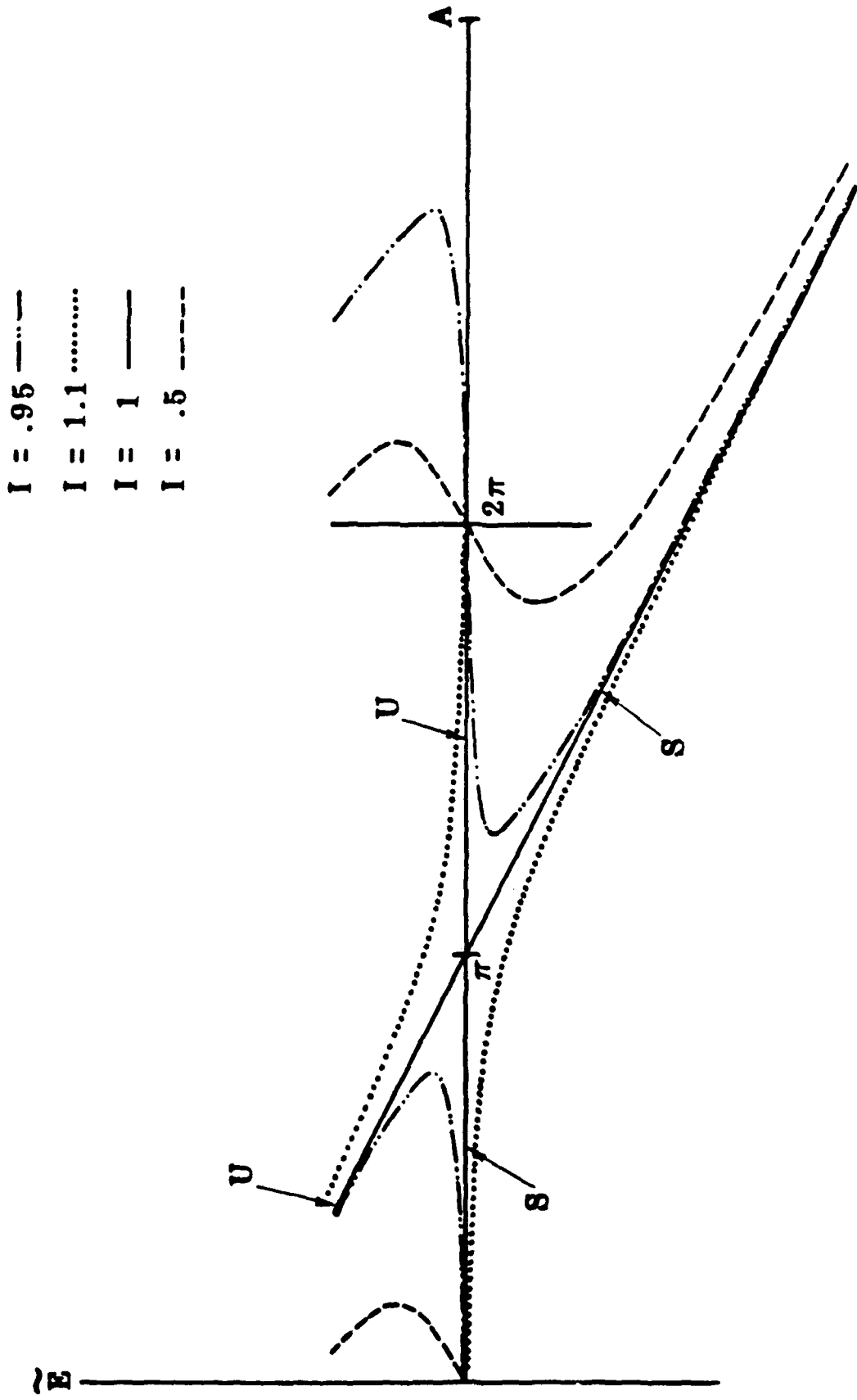


Figure 10. Curves of scaled electric field at the injection plane, E , versus scaled current, A , for various values of charge neutralization, I . The curves represent slices through a 3-dimensional surface. The S and U indicate stable and unstable branches for the $I=1$ slice.

$d\alpha/dE_0 = 0$. We shall carry out the analysis for $I = 0$, but our method can be applied to any similar jump phenomenon.

A linear stability analysis⁶ about the steady state described by (20) results in the dispersion relation

$$(2 + \beta) e^{-\beta} = 2 - \beta + \frac{\beta^3}{\alpha^2 t_0^3} \quad (24)$$

where $\beta = i\omega t_0$. We have written the expression derived in Reference 6 in terms of our dimensionless variables. For α near the SCL value we let

$$\alpha = \frac{4}{3} - \epsilon^2, \quad \epsilon \ll 1. \quad (25)$$

and find from (20) that near this value, t_0 is approximately

$$t_0 = \frac{3}{2} \mp \epsilon \frac{3}{2\sqrt{2}} + O(\epsilon^2) \quad (26)$$

where the $-(+)$ sign corresponds to the lower (upper) branch in Fig. 9.

By substituting in (24), and assuming β small, we find that

$$i\omega = \beta \approx \mp 2\sqrt{2} \epsilon + O(\epsilon^2) \quad (27)$$

Since the linearized analysis led to time factors of the form $e^{i\omega t}$ in the perturbations, it follows that the lower branch in Fig. 9 is stable and the upper unstable, while at the SCL ($\epsilon = 0$) we have neutral stability.

Above the value $\alpha = 4/3$, linearized theory is not applicable. Utilizing multiple scaling perturbation theory⁴⁴ we can carry out a nonlinear

stability analysis near $\alpha = 4/3$. In system (15) we set $\alpha = 4/3 \pm \epsilon^2$. In this neighborhood perturbations evolve on a "slow" time scale, depicted by $\tau = \epsilon t$.

Eliminating the electric field by combining (15b) and (15c) and utilizing τ , system (15) becomes

$$\epsilon n_{\tau} + (nu)_x = 0 \quad (28a)$$

$$(\epsilon u_{\tau} + uu_x)_x = - \left(\frac{4}{3} \pm \epsilon^2\right)^2 n \quad (28b)$$

with conditions $u(0, \tau) = 1$, $n(0, \tau) = -1$ and $\int_0^1 E dx = 0$ rewritten as

$$\epsilon \int_0^1 u_{\tau} dx + \frac{1}{2} [u^2(1, \tau) - u^2(0, \tau)] = 0 \quad (29)$$

Substituting the asymptotic expansions

$$u = \sum_{i=0}^j \epsilon^i u_i(x, \tau) + O(\epsilon^{j+1}), \quad n = \sum_{i=0}^j \epsilon^i n_i(x, \tau) + O(\epsilon^{j+1}) \quad (30)$$

for u and n into (28) and equating coefficients of various powers of ϵ , there results a hierarchy of equations for the u_i and n_i .

Solving the $O(1)$ system gives

$$(u_0 - \frac{1}{2})(u_0 + 1)^2 = 2(2x - 1)^2 \quad (31a)$$

$$n_0 = -1/u_0 \quad (31b)$$

To solve the $O(\epsilon)$ system we introduce a new variable q by

$$x = \frac{16}{9} \left(\frac{q^3}{6} - \frac{3}{8} q^2 \right) + q \quad (32)$$

so that

$$u_0 = \frac{16}{9} \left(\frac{q^2}{2} - \frac{3}{4} q \right) + 1 \quad (33)$$

We then find

$$n_1 = \frac{1}{u_0^2} u_1 \quad (34a)$$

$$u_1 = C \frac{q(q - 3/2)}{u_0} \quad (34b)$$

with C a constant of integration which is, in general, a function of the slow time τ . To find $C = C(\tau)$ which determines the slow evolution of the perturbation $u_1(x, \tau)$ we need to go to the next order, $O(\epsilon^2)$. By

substituting in the expressions for u_0 , u_1 , n_0 , n_1 and eliminating n_2 , we find that $u_2(x, \tau)$ satisfies

$$\begin{aligned} (u_0 u_2)_{xx} + \frac{16}{9} \frac{1}{u_0^2} u_2 &= \frac{16}{9} \frac{C_\tau}{u_0} \int_0^q \frac{q(q-3/2)}{u_0^2} dq + C^2 \frac{q^2(q-3/2)^2}{u_0^3} \\ &- C_\tau \left(\frac{q(q-3/2)}{u_0} \right)_x = \frac{8}{3} \frac{1}{u_0} \end{aligned} \quad (35a)$$

$$u_2(0, \tau) = 0, \quad u_2(1, \tau) = + \frac{9}{16} C_\tau \quad (35b)$$

The solution to this inhomogeneous two-point boundary value problem exists provided a certain orthogonality condition between the right hand side and the solution of the adjoint problem that takes account of the boundary conditions is satisfied (Fredholm alternative theorem).⁴⁵ This leads to the desired equation determining $C(\tau)$:

$$aC_{\tau} + bC^2 \pm c = 0 \quad (36)$$

where a , b , and c are found to be

$$a = - \int_0^{3/2} \frac{q(q-3/2)}{u_0^2} \left[\frac{16}{27} q^2 (q - 9/4) + \frac{3}{2} \right] dq = 1.6850 \quad (37a)$$

$$b = \frac{8}{3} \int_0^{3/2} \frac{q^3 (q-3/2)^3}{u_0^4} dq = - 3.7968 \quad (37b)$$

$$c = \frac{8}{3} \int_0^{3/2} q(q-3/2) dq = -1.5 \quad (37c)$$

In (36) the (+) or (-) signs indicate that we are above or below the SCL, respectively.

Above the SCL, we find

$$C(\tau) = - \frac{c}{b} \tan \left[\sqrt{cb} \left(\frac{\tau + \tau_0}{a} \right) \right] \quad (38)$$

and below

$$C(\tau) = \frac{c}{b} \tanh \left[\sqrt{cb} \left(\frac{\tau + \tau_0}{a} \right) \right] \quad \text{if} \quad |C(0)| < \sqrt{c/b} \quad (39)$$

$$C(\tau) = \frac{c}{b} \coth \left[\sqrt{cb} \left(\frac{\tau + \tau_0}{a} \right) \right] \quad \text{if } |C(0)| > \sqrt{c/b} \quad (40)$$

where τ_0 is a constant of integration. In general, small initial perturbations will lead to the solution

$$u(x,t) = u_0 + \sum_{i=1}^j C_i(\tau) e^{\omega_i t} u_i(x) + O(\epsilon^2) \quad (41)$$

where ω_i are the various distinct solutions of the dispersion relation (24) at $\alpha = 4/3$.^{44,46} It is straightforward to show that all modes are such that $\text{Re}(\omega_i) < 0$ except one for which $\omega = 0$. Thus, all other modes will decay in the fast time scale and only the neutral mode ($\omega = 0$) will persist. Our solution after a short time will look like

$$u = u_0 + \epsilon C(\tau) \frac{q(q - 3/2)}{u_0} + O(\epsilon^2) \quad (42)$$

From the given initial conditions it is easy to determine the initial condition for the neutral mode. Below the SCL, if the initial conditions are such that $C(0) > -\sqrt{c/b}$, the solution will evolve to the stable lower branch in Fig. (9) (Region I), while if $C(0) < -\sqrt{c/b}$, $C \rightarrow \infty$ in finite time. (Fig. 9, Region II). Blow up in finite time also occurs above the SCL for any $C(0)$. This does not mean that the actual solution blows up, just that it evolves to a final state far away from the two steady branches shown in Fig. (9), and thus, is not accessible by perturbation theory.

As can be seen in (38), the blow up above the SCL is described by a tangent function, therefore, the growth rate we find for this case must be appropriately interpreted. Note that the linearized dispersion relation

seems to suggest an imaginary exponential growth rate above the space charge limit.^{3,6} In view of our results, we see that this is actually misleading. Moreover, we find that even below the SCL the stable steady branch can be destabilized by sufficiently large perturbations.

Our results agree with the linear theory, provided we consider the limit where the latter becomes applicable. Thus, we must compare the linear theory with (39) as $\tau \rightarrow +\infty$ (near the stable branch) and (40) as $\tau \rightarrow -\infty$ (near the unstable branch). To demonstrate this we set $\tau = \epsilon t$ in (39) and consider the limit $t \rightarrow +\infty$. Then

$$\begin{aligned}
 C(t) &= \frac{c}{b} \tanh \left[\frac{\sqrt{cb}}{a} (\epsilon t + \tau_0) \right] \\
 &= \frac{c}{b} \left\{ \frac{1 - \exp - \left[\frac{2\sqrt{cb}}{a} (\epsilon t + \tau_0) \right]}{1 + \exp - \left[\frac{2\sqrt{cb}}{a} (\epsilon t + \tau_0) \right]} \right\} \\
 &= \frac{c}{b} \left\{ 1 - 2 \exp - \left[\frac{2\sqrt{cb}}{a} (\epsilon t + \tau_0) \right] + \dots \right\} \quad (43)
 \end{aligned}$$

We see that the decay rate of the perturbations as $t \rightarrow +\infty$ is equal to

$$\frac{2\sqrt{cb}}{a} \epsilon \approx 2.83\epsilon \quad (44)$$

which is the same as that found by the linearized analysis.⁶ This quantity is important as it also determines an initial "growth rate" for the jump instability above the SCL described by (38). If we substitute the original dimensional time variable into our expressions and write the deviation of α from its value at the SCL as

$$\epsilon = (\alpha - \alpha_{SCL})^{1/2} = (\alpha - \frac{4}{3})^{1/2} \quad (45)$$

we find that the "growth rate" is given by

$$D = (\alpha - \frac{4}{3})^{1/2} \frac{\sqrt{cb}}{a} \frac{v_0}{l} \quad (46)$$

or

$$D = \left(\frac{l \omega_p}{v_0} - \frac{4}{3} \right)^{1/2} \sqrt{2} \frac{v_0}{l} \quad (47)$$

Of course, for the expansions in (41) to be valid, we must have $C(\tau) \ll 1/\epsilon$. However, while C is not too large (38) gives a reliable estimate for the growth rate of the instability.

IV. MICROWAVE GENERATION

Of the several millimeter sources that are in various stages of development (see Figure 11), the virtual cathode oscillator (Vircator) has a combination of characteristics which recommend it for high frequency use. First, the frequency of the vircator is tunable by changing the magnitude of an imposed axial magnetic field, eliminating any requirement to change the physical structure of the device. A single vircator will be tunable over an order of magnitude in frequency (e.g., 10 GHz - 100 GHz). Second, the bandwidth of the generator can be narrow or broad based on magnetic field shaping. Third, because the vircator functions above the space-charge limiting current for the electron beam, given efficient operation, it should be capable of much higher power than other microwave sources. Finally, the lack of passive resonating structures to produce the transmitted wave reduces the problem of field emission. This also increases the maximum possible generator power.

Experimentally, the virtual cathode has already proven itself to be a copious microwave source.^{22-24,26,47} Table 4 lists experiments which have been carried out to date. With the exception of the Didenko experiment at Tomsk,²⁶ the frequency spectra have all had a broad bandwidth and relatively low efficiency. Nevertheless, even at low efficiency the experiment at Harry Diamond Laboratories⁴⁷ using a foilless diode (1 MV, 30 kA) produced 3 GW of power in the Ku band. It is one of the most powerful centimeter wavelength microwave sources available. The experiments at the Naval Research Laboratory²² (Mahaffey et al.) and Tomsk will be reviewed in detail, because these experiments had the most useful diagnostics. Based on analytical work and computer simulations these experimental results can now be explained. It will be shown later that the foilless diode in a shaped axial magnetic field represents the best configuration for a high frequency device.

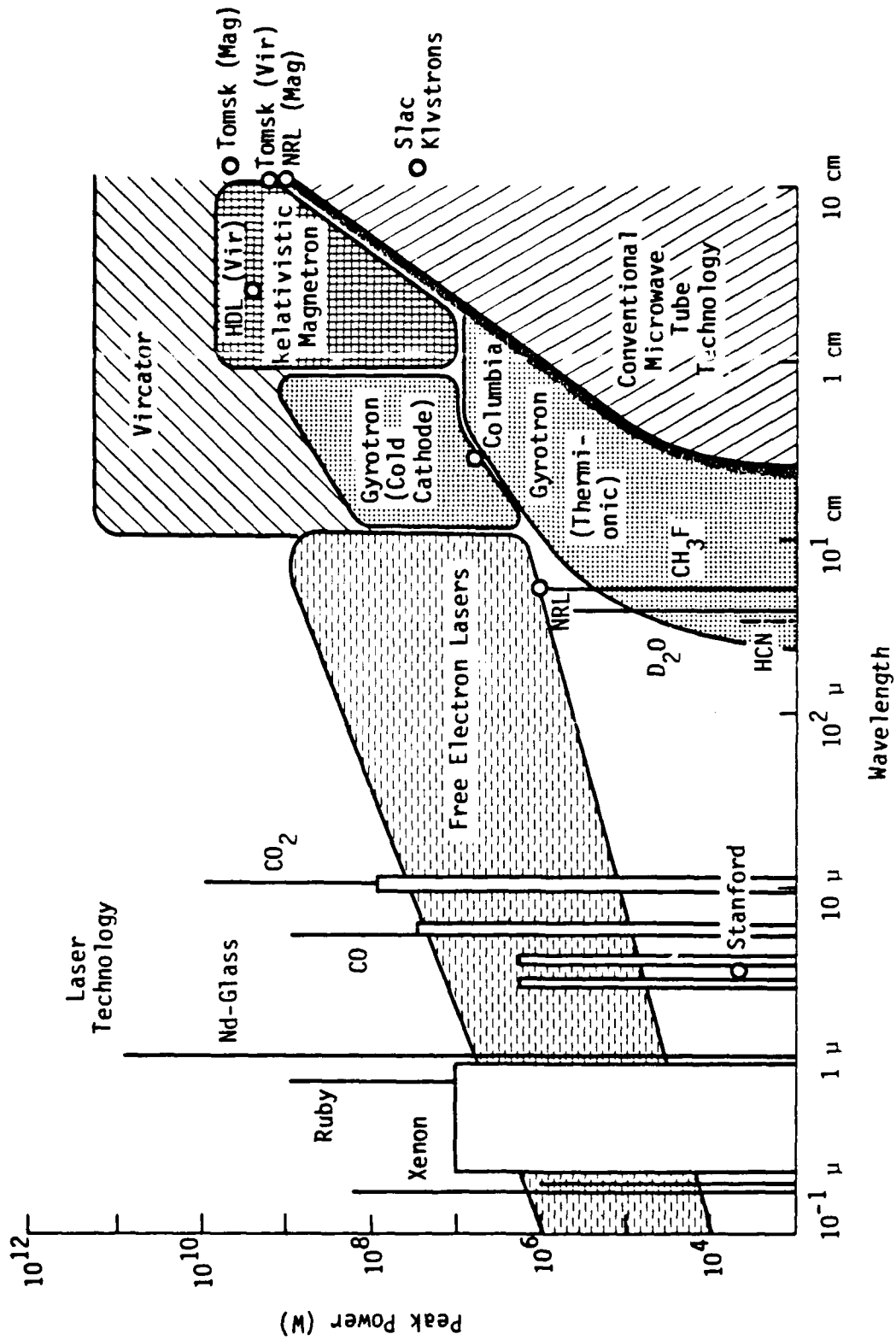


Figure 11. Anticipated optimal operating ranges for various sources of high power electromagnetic radiation. Several experimental points are included.

TABLE 4

HIGH POWER MICROWAVE GENERATION HAS BEEN WITNESSED IN VARIOUS ELECTRON BEAM CONFIGURATIONS WHEN VIRTUAL CATHODES ARE FORMED.

REFERENCE	SYSTEM	PEAK POWER	FREQUENCY	EFFICIENCY
1. MAHAFFEY, et al.	REFLEX TRIODE	100 MW	11 GHz * (10.0 - 12.4 GHz)	1.5%
2. BRANDT, et al.	REFLEX TRIODE	---	9.8 GHz * (7.0 - 13.0 GHz)	---
3. BUZZI, et al.	FOIL DIODE	1 GW	10 GHz * (9.0 - 14.0 GHz)	1.25%
4. DIDENKO, et al.	REFLEX TRIODE	1.4 GW	3.3 GHz * (2.1 - 5.0 GHz)	12%
5. BROMBORSKY, et al.	FOILLESS DIODE	3 GW	15 GHz * (8.2 - 18.0 GHz)	5%
6. CLARK, et al.	FOILLESS DIODE	---	WIDEBAND * (1.7 - 40.0 GHz)	---
7. EKDAHL, et al.	FOILLESS DIODE	> 100 MW	> 70 GHz	---

* DETECTOR BANDWIDTH IN PARANTHESES

Although only scaling relations are presently available, qualitative dependencies of virtual cathode parameters on beam kinetic energy and injected current are known.

1. Potential amplitude, position, and oscillation frequency all have the same functional dependence on injected beam current. The positional dependence of the virtual cathode is given in Figure 12 for a 50 kV diode.
2. These parameters asymptotically approach a limiting value for current above the space-charge limit.
3. The fundamental oscillation frequency is approximately the relativistic beam plasma frequency given by

$$\omega_p^0 = \left(\frac{4\pi n_b^0 e^2}{\gamma_0^3 m} \right)^{1/2} \quad (48)$$

where n_b^0 is the electron beam number density at injection. In particular the oscillation frequency from numerical simulations varies such that

$$\omega_p^0 \leq \omega_{osc} \leq \sqrt{2\pi} \omega_p^0 \quad (49)$$

The end result is creation of an electrostatic potential minimum which oscillates in time and space. This fluctuating potential barrier acts as a gate to reflect some electrons and transmit others. The motion

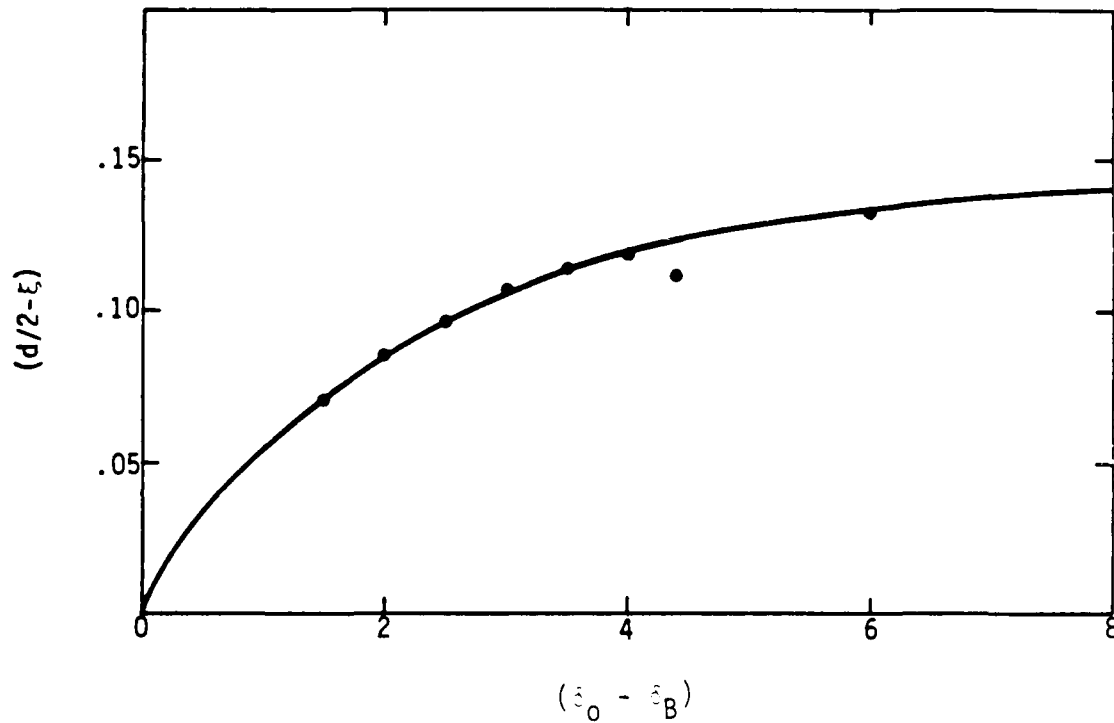


Figure 12. Variation of virtual cathode distance, ξ , from the one-dimensional diode center versus the difference between the injected current, δ_0 , and the current needed for bifurcation, δ_B , in units of the Child-Langmuir value. δ_B is assumed to have a value of 4 from the classical analysis.

of the gate bunches charge. However, the charge bunch and virtual cathode are separated spatially as shown in Figure 13.

By analogy this configuration represents an LC oscillator. The virtual cathode acts as a capacitor to store the beam kinetic energy. During that portion of the limit cycle in which the potential is greater than the injected beam energy, charge is constrained to remain near the anode. This starves the virtual cathode so that its amplitude decreases below $(\gamma_0 - 1) mc^2/e$. Once this occurs the charge bunch is transmitted. The electron motion represents a large time varying current through an inductor. The presence of charge away from the anode reestablishes the virtual cathode, and the cycle repeats. The effect on beam current can be examined using simulations. A net current diagnostic is given in Figure 14 where the probe is positioned between the anode and virtual cathode. The injected current in units of mc^3/e , v_0 , is three times the limiting current, v_L , and γ_0 is 5. Note that the virtual cathode can actually reverse the direction of current. The average current value is v_L .

The oscillating current generates microwaves.²⁵ The wave frequency is the oscillation frequency of the virtual cathode. The wave propagates down the drift tube in a TM waveguide mode, which determines the wavelength and phase velocity of the wave in the guide. The field configuration is evident in simulations where there is no axial magnetic field. If a cold beam is injected and azimuthal symmetry is assumed by the code, the only nonzero fields are E_z , E_r , and B_θ in cylindrical geometry. These three fields define a TM wave traveling in the z direction. A time history and frequency spectrum of the B_θ field downstream of the virtual cathode is given in Figure 15. The oscillation frequency of the virtual cathode and its first three harmonics are clearly visible. Also included is a history of the E_z field on axis later in time. The

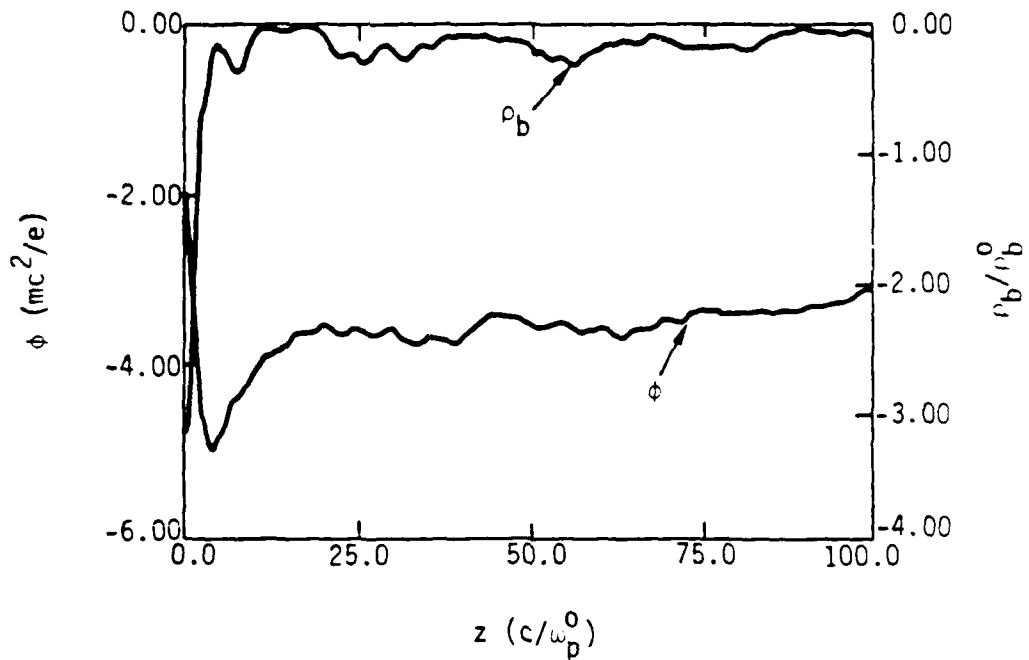


Figure 13. CCUBE diagnostic of charge density, ρ_b , and potential, ϕ , as a function of a longitudinal distance, z , for an electron beam in a two-dimensional drift space with an imposed large axial magnetic field. ρ_b is normalized to its value at injection. The value of (γ_0-1) is 4. Note that the minimum charge density and potential are separated in z .

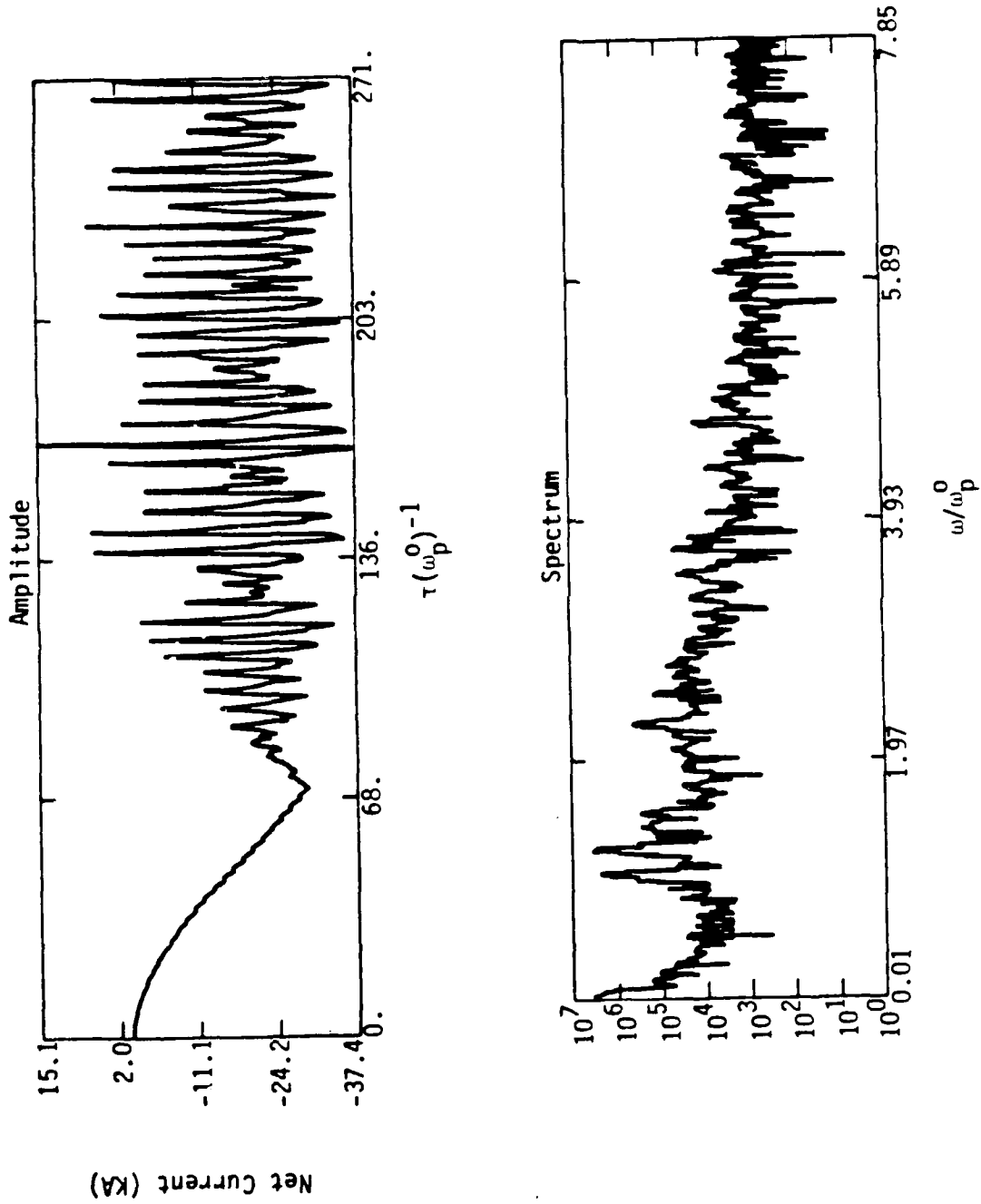


Figure 14. Net current amplitude and spectrum for a probe placed between the anode and virtual cathode. $\gamma_0 = 5$ and $v_0 = 3 v_{\phi}$.

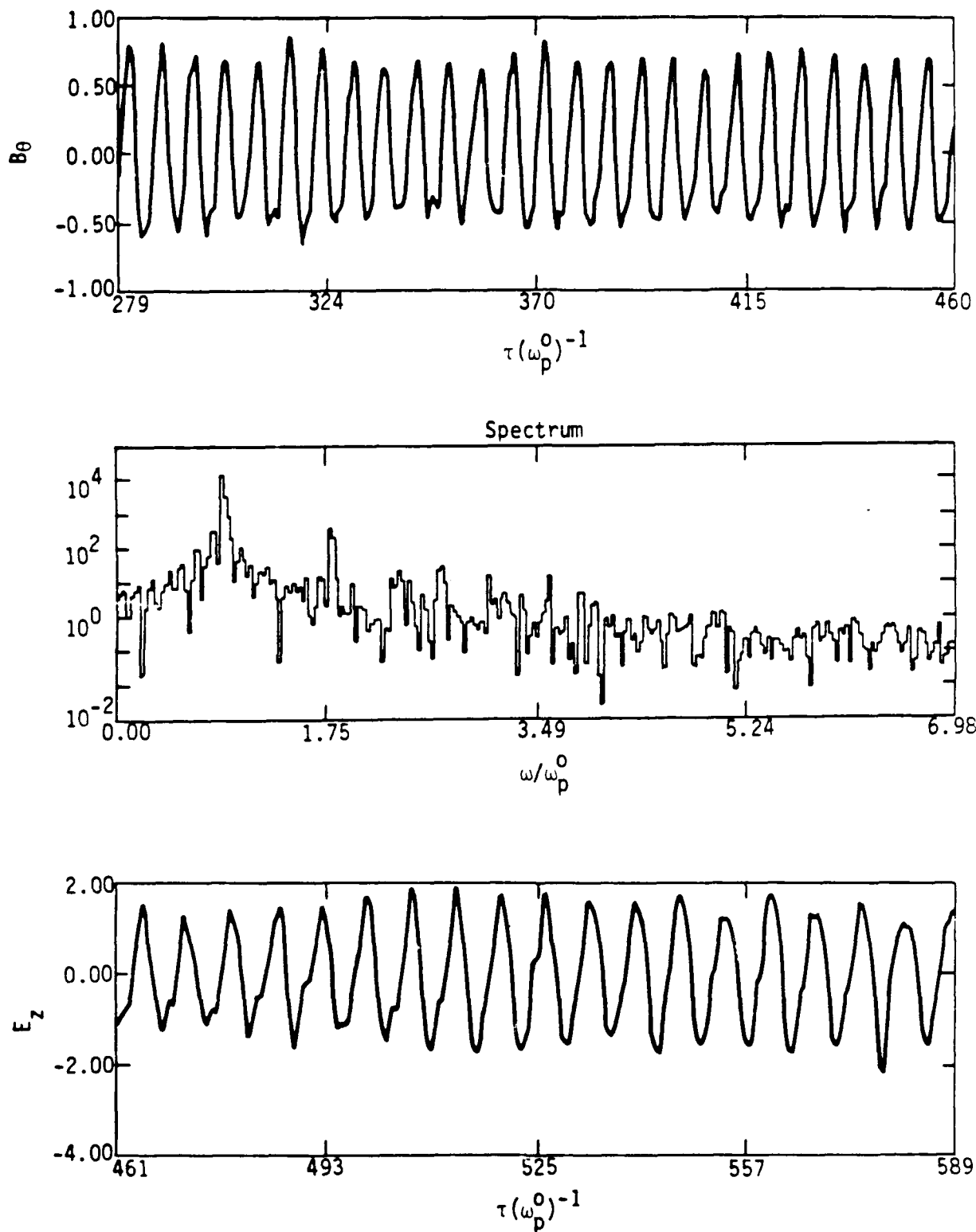


Figure 15. B_θ and E_z field probe histories and frequency spectrum for a simulation with $\gamma_0 = 5$, $\nu_0 = 3.7$ and $B_z = 0$. Field units are MeV/cm for a beam density of 10^{12} .

frequency spectrum, which is not included, is almost identical to that of B_0 . No attenuation of the field strengths is noted over the length of the drift tube which is equivalent to one meter for a beam density of 10^{12} cm⁻³. The waveguide mode is TM_{02} with an RF conversion efficiency of greater than 20%. Because there is no axial magnetic field in this case few electrons are transmitted to the end of the drift tube. The loss of transmitted electrons does not reduce the RF efficiency.

As noted earlier, several experiments have already generated high power microwaves from virtual cathodes. The most informative experiments took place at the Naval Research Laboratory and at the Institute of Nuclear Physics at Tomsk. Both experiments used a reflex triode configuration. The electron beam machines were almost identical (350 kV, 50 kA versus 450 kV, 65 kA). Some salient features were

1. The average microwave frequency increased as the square root of triode voltage, V (see Figure 16).
2. Enlarging the anode cathode gap spacing, d , decreased wave frequency.
3. The microwave bandwidth is related to the change in voltage over the beam pulse, $\Delta V/V$. In the Russian experiment where $\Delta V/V = 5\% - 10\%$ the power FWHM occurred at $\pm 10\%$ of the peak frequency.
4. For a constant voltage the frequency decreased as cathode shape was changed from solid to thick annular and finally thin annular plates of comparable area.

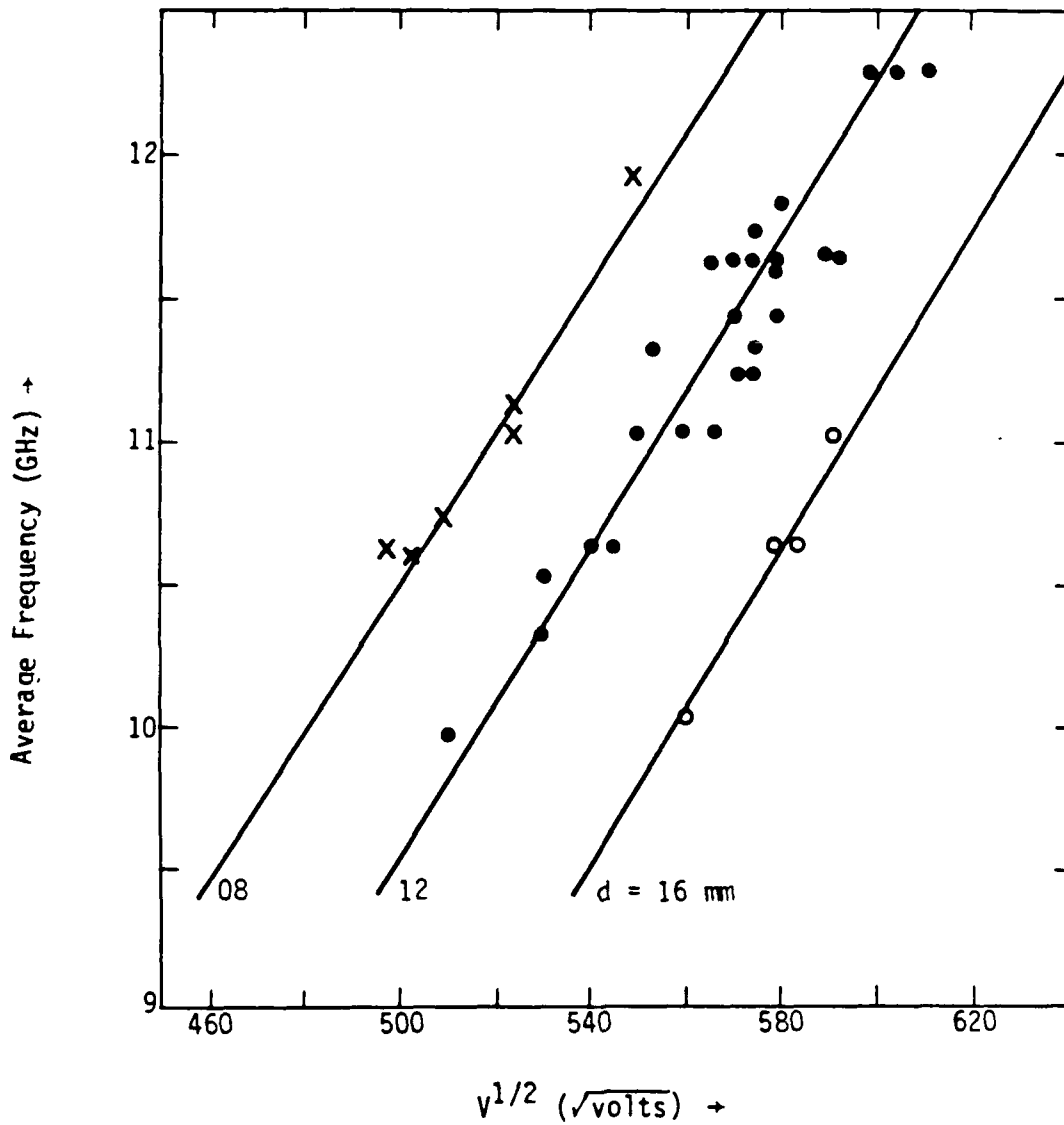


Figure 16. Average microwave frequency dependence on the square root of triode voltage (after Mahaffey et al.).

5. The imposition of an axial magnetic field greatly decreased the RF signal detected.

Each result can be explained in terms of virtual cathode characteristics. For a nonrelativistic beam in a semi-infinite one-dimensional drift space the vircator frequency, ω_{osc} , is directly proportional to the beam plasma frequency given by Equation 48. This is a good approximation for both experiments being considered here, because the beams are of low energy and the drift tube length is much greater than its radius. Therefore, $\omega_{osc} \propto n_b^{1/2}$. The current density extracted from the cathode is defined by the nonrelativistic Child-Langmuir relation, which is

$$j_{CL} = \frac{4}{9} \left(\frac{2e}{m} \right)^{1/2} \frac{v^{3/2}}{4\pi d^2} = n_b e v \quad (50)$$

An expression for velocity is obtained from conservation of energy. It is

$$v = \left(\frac{2e}{m} \right)^{1/2} V^{1/2} \quad (51)$$

Combining Equations 3 and 4 and solving for n_b , one obtains

$$n_b = \frac{1}{9\pi e} \frac{V}{d^2} \quad (52)$$

or

$$\omega_{osc} \propto \omega_b = \frac{2}{3} \left(\frac{e}{m} \frac{V}{d^2} \right)^{1/2} \quad (53)$$

Thus, $\omega_{osc} \propto (V/d^2)^{1/2}$, which is precisely the experimental result. In addition, this dependence of vircator frequency on voltage explains the importance of a flat top voltage pulse in producing a narrow bandwidth. The closure of the A-K gap, which is due to plasma motion inherent in any foil system, also makes the spectrum broader. The Tomsk experiment used a mesh anode which would minimize the latter effect. An expression for these observations, which is obtained by differentiating Equation 53, is

$$\frac{\Delta\omega_{osc}}{\omega_{osc}} = \frac{\Delta V}{2V} + \frac{\Delta d}{d} \quad (54)$$

Cathode shape plays a role in defining the space-charge limiting current via a two-dimensional geometrical factor. The value of v_g for a solid beam is less than for a thin annular beam of the same energy, current, and area. In the solid beam case the position of the virtual cathode is closer to the anode. This leads to a higher oscillation frequency, because the electron transit time between the anode and virtual cathode is less.

The final characteristic of the experiments is the apparent reduction of microwave generation in the presence of an axial magnetic field. However, two dimensional simulations, which include the diode physics, show that microwaves are still being produced.⁴⁸ The magnetic field forces the reflected electrons to reenter the A-K gap region along field lines. In the case of a foil diode or reflex triode the electrons suffer energy losses and are scattered by the foil. After several foil transits the beam electron distribution is nearly Maxwellian. This is equivalent to having electrons of widely varying voltage interacting with the virtual cathode. Thus, an extremely broad RF spectrum is produced which greatly reduces the detectable signal in any particular frequency band. The same result also occurs in foilless diodes. The broad electron

velocity distribution results from a two stream instability between particles with positive and negative axial velocities in the region between the real and virtual cathodes. The instability heats the two beams until there is a homogeneous electron distribution in velocity space.

Based on our current theoretical knowledge of the virtual cathode, numerical simulations, and experimental results, the following points must be considered in the design of a coherent, high frequency vircator.

1. Both the oscillation frequency and net current asymptotically approach a value as injected current is increased above the space-charge limit. Thus, using a large value of v_0/v_z does not substantially increase frequency or RF efficiency where efficiency is given by

$$\eta \leq \frac{e\Delta\phi}{(\gamma_0-1) mc^2} \quad (55)$$

A foilless diode in a strong axial magnetic field produces a very thin annular beam. Since v_z for an annular beam is larger than for a solid beam of the same area, the value of v_0/v_z will be smaller for the same beam current.

2. Generation of high microwave frequencies requires large beam densities. Extremely high beam densities ($n > 10^{14} \text{ cm}^{-3}$) have been obtained from a foilless diode.⁴⁸ The beam plasma frequency scales linearly with the electron cyclotron frequency due to the magnetic field.⁴⁹

3. The following characteristics must be met to assure narrow bandwidth microwave generation from the vircator.
- a) No reflexing of electrons in the region between the real and virtual cathodes must occur. Any axial magnetic field must be shaped to divert the electrons, or flux excluders must be employed to confine the magnetic field to the diode region. The latter arrangement will allow the radial space-charge electric field to perform the role of expelling electrons to the waveguide wall.
 - b) The electron beam must be cold. Experimental⁵⁰ and theoretical⁴⁹ results indicate that foilless diodes create low emittance beams. Laminar flow, where the electron Larmor orbit is smaller than the beam thickness, is obtained when⁵⁰

$$\omega_c > (\gamma_0 - 1)^{1/2} \frac{c}{\sqrt{a\delta/Z}} \quad (56)$$

where a is the orbit radius, δ is the radial spacing between the cathode and drift tube wall (which acts as the anode) and ω_c is the electron cyclotron frequency given by eB_z/mc . Low beam scatter is also assured, because of the lack of a foil.

- c) The diode voltage and injected current must be constant. Flat-top voltage pulses can be attained in a variety of ways in several diode configurations. However, absence of diode closure in some foilless diode experiments makes a long pulse device possible. Also, at high voltages the foilless diode operates as a purely resistive load,

therefore $\omega_{osc} \propto \sqrt{\frac{I}{V}} = \sqrt{Z}$ is constant.

It is evident from this discussion that the foilless diode in a strong axial magnetic field represents the optimal configuration for a high frequency vircator. It optimizes microwave power and efficiency while generating high frequency, coherent radiation.

V. Experimental Apparatus

1. Introduction

This section describes the VIRCATOR experimental apparatus in detail. The general design philosophy has been to include as much flexibility as possible in the mechanical and electrical systems. This approach allows for the inevitable changes in experimental geometry and diagnostics to be made easily, and will also permit a straight-forward maximization of the output microwave power over the various degrees of freedom available.

Mechanical aspects of the experiment are described in Section 2. Included are the vacuum vessel design and descriptions of the anode positioning assembly and the cathode. Electrical systems are summarized in Section 3. Electronic schematics for the pulsed 50 kilogauss magnet power supply and for the lumped element Blumlein electron beam driver are presented. Diagnostics of the pulsed power systems and of the electron beam are also described. Measurements of the microwave emission power spectrum will be made with the microwave spectrometer described in Appendix A.

2. Mechanical Design

The successful operation of the VIRCATOR device requires that the electrostatic potential surfaces have a particular structure, and that these equipotential surfaces be appropriately oriented with respect to the applied magnetic field. These criteria will be satisfied if the cathode, anode, annular limiter, and solenoidal magnetic field are aligned concentrically, and if all are cylindrically symmetric. However, the required accuracy of this concentric relationship has yet to be thoroughly investigated, since it requires making several runs of a fully three-dimensional simulation code. Rather than attempt to fabricate the entire experiment to

exacting tolerances, it was therefore decided to build a mechanical system capable of changing the geometrical relationships between the various components in small incremental steps. This approach allows performance of the experiment to be optimized in a systematic fashion, and will also provide a measurement of the system sensitivity to geometrical relationships between the components.

Vacuum System

The components associated with electron beam production are enclosed in a standard 18 inch diameter bell jar vacuum system, and pumped by a NRC 4 inch diffusion pump to a base pressure less than 10^{-6} torr. In order to allow for high voltage and mechanical vacuum feedthroughs, a custom stainless steel collar, designed by MRC and fabricated by Huntington Mechanical Laboratories, is positioned between the baseplate and glass bell jar. Design drawings for this unit are shown in Figure 17. Conflat type vacuum flanges are used on all ports because of the wide variety of electrical and mechanical feedthroughs manufactured for this style flange. Use of off-the-shelf type hardware yields cost savings and increased system flexibility relative to custom machined vacuum feedthroughs.

The experiment is arranged on the feedthrough collar of Figure 17 as follows. A 135 kV high voltage feedthrough (Ceramaseal Inc. #908C1854-1) is mounted on vacuum port 1, positioning the carbon cathode at approximately 5 cm from the center of the chamber. The pulsed magnet is mounted to the stainless steel brackets shown so that it is concentric with the cylindrical cathode. The brackets are slotted to allow for magnet positioning along its axis; vertical adjustments are made by screws in the magnet base. The beam target assembly, consisting of the stainless steel anode, annular limiter, and waveguide entrance port, is located concentrically with the cathode and magnet by means of a positioning assembly

FEEDTHROUGH COLLAR

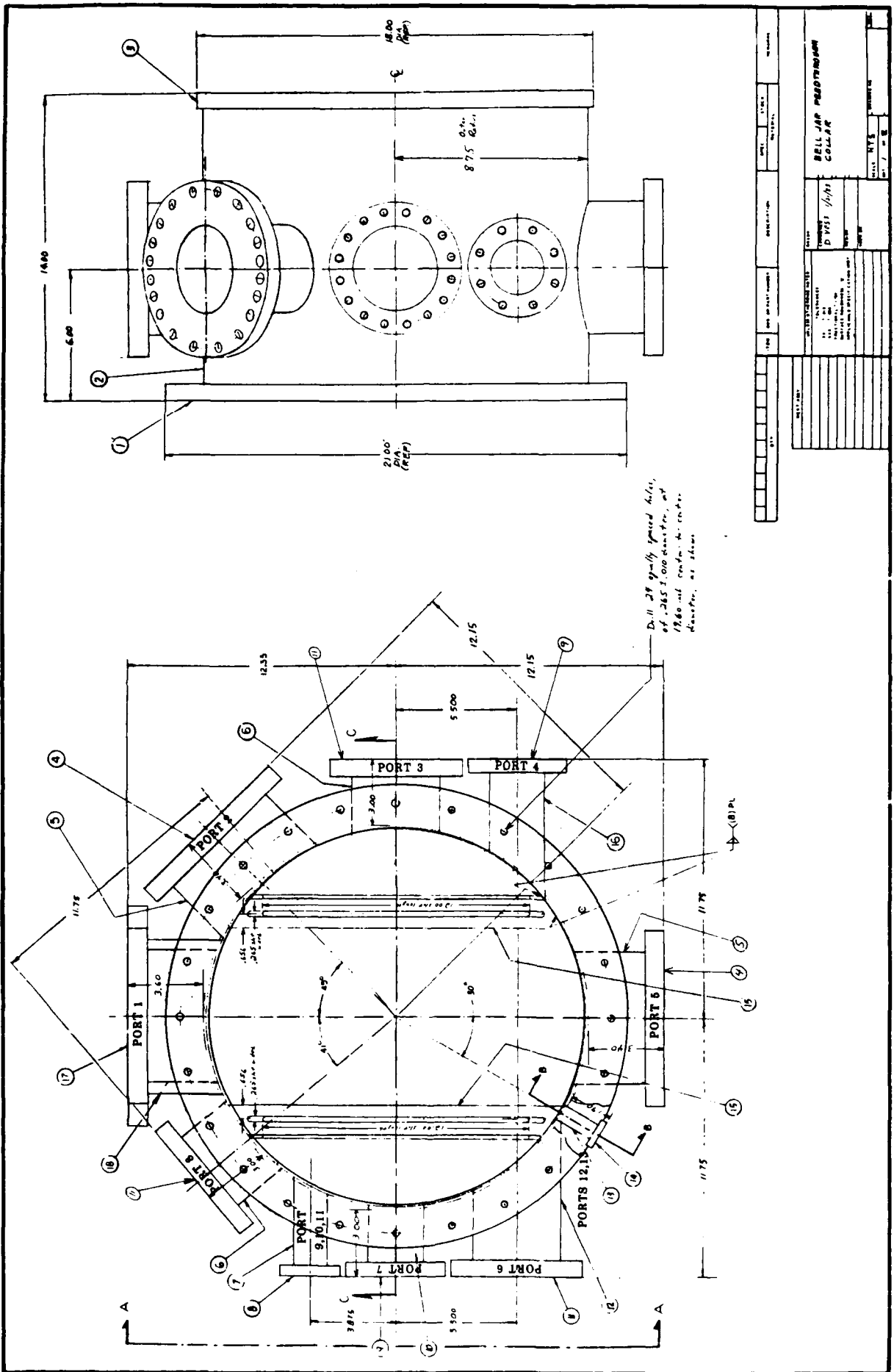


Figure 17. Fabrication drawing of the VIRCATOK vacuum vessel. All flanges are Conflat type to accept standard feedthrough hardware.

FEEDTHROUGH COLLAR

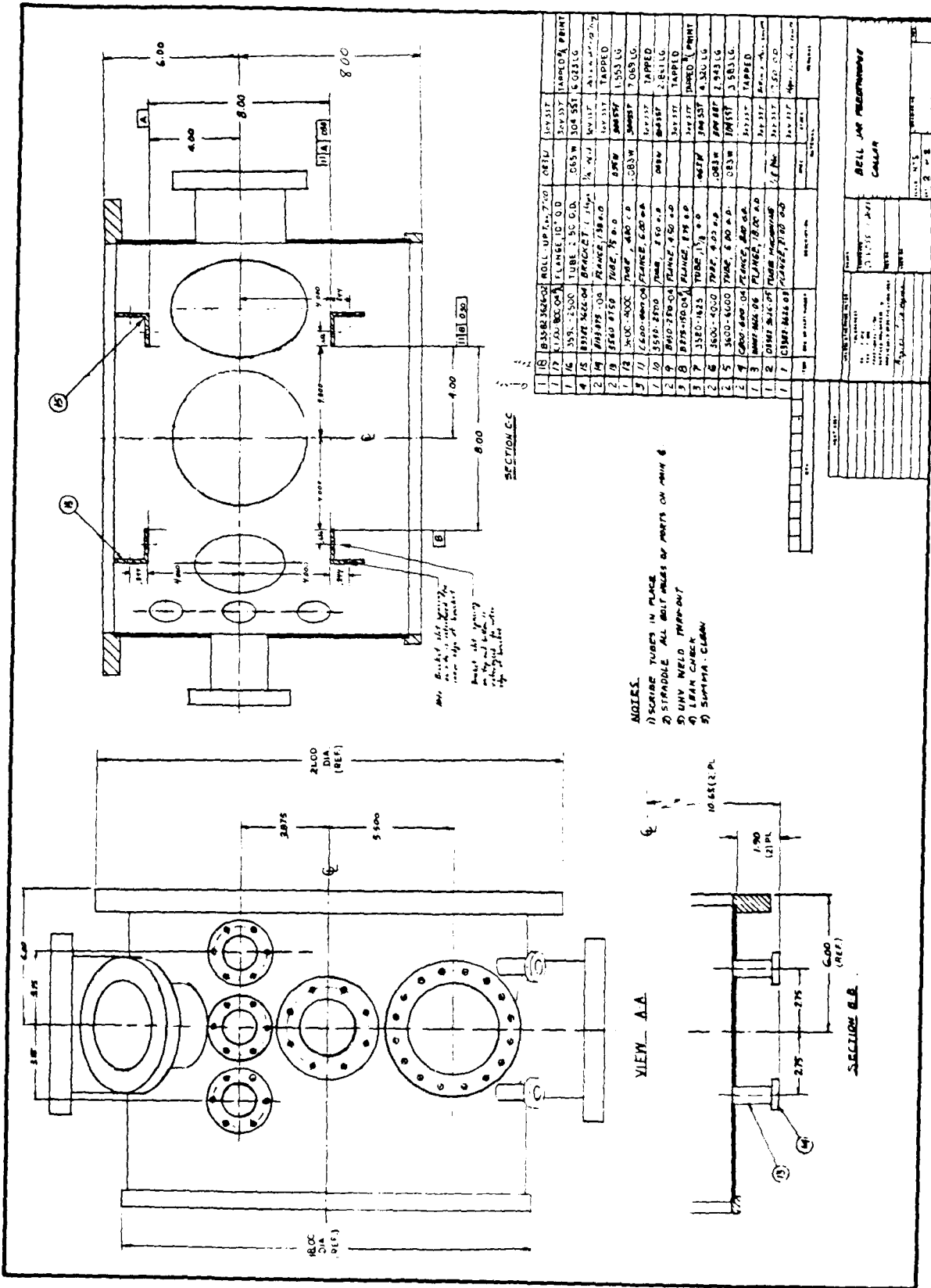


Figure 17. Concluded.

mounted in vacuum port 3. Microwave emission into the microwave spectrometer is through vacuum port 5. The remaining vacuum ports accommodate the electrical and mechanical feedthroughs related to beam and microwave diagnostics.

Beam Target Assembly

The ideal experimental configuration would allow manipulation of the various electrical components from outside the vacuum vessel, eliminating the need to break vacuum when an adjustment is required. Because mechanical motion vacuum feedthroughs are costly, the design allows only the beam target assembly, consisting of the anode, annular limiter, and the waveguide entrance port, to be manipulated from outside the vacuum vessel. A commercial micrometer positioning assembly capable of 100 micron spatial resolution (Huntington Mechanical Laboratories #PM-600-XYZTR) has been chosen for this application. This unit allows full 5 degree-of-freedom motion of the target assembly relative to the cathode.

The relative geometry of the cathode, beam target assembly, and magnet is shown in Figure 18. The cathode consists of a hollow carbon rod of outside diameter 0.70 cm with a 0.08 cm diameter wall. Two characteristics make carbon a strong choice for the cathode. First, its high resistivity allows magnetic field penetration on a sub-microsecond time scale, ensuring that the magnetic field lines will be nearly normal to the cathode surface at the time that the beam fires. Second, it has a low macroscopic electric field threshold for field emission, of order 10 kV/cm⁵¹. However, for the design operating voltage of 50 kV, the electric field at the cathode surface is 625 kV/cm, ensuring that cathode field emission can be obtained at substantially lower voltages and promoting uniform field emission. The purpose of the thin cathode wall is to promote formation of an annular electron beam by eliminating emission from the cathode center.

BEAM TARGET ASSEMBLY

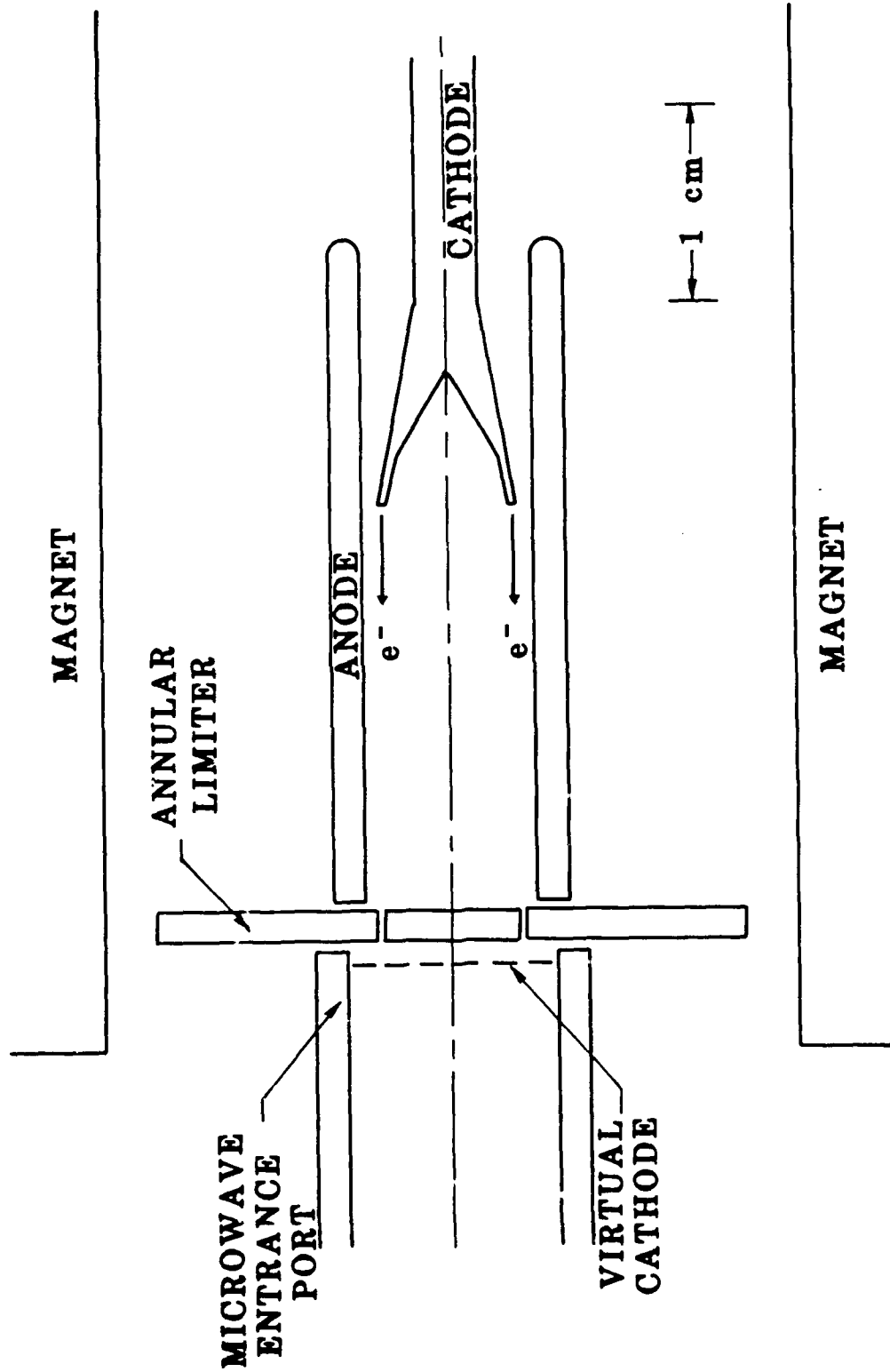


Figure 18. Sketch of the beam target assembly. The anode, annular limiter, and microwave entrance port are operated at ground potential, and the cathode is operated at negative high voltage.

In order to maximize the space-charge limited current emission from the cathode, the cylindrical anode of inside diameter 0.43 cm surrounds the cathode with a narrow 0.08 cm gap. This geometry yields a diode impedance for a 50 kV beam of 66 ohms, with a space-charge limited current of 760 amps. The annular limiter serves a dual role. It acts as ground plane for electron beam production in the source region and also prevents electrons reflected from the virtual cathode from re-entering the source region. Beam equilibrium considerations dictate an axial spacing between the annular limiter and cathode of several anode radii, yielding a design gap of 2.0 cm. The radial gap of the annular limiter is chosen to match the expected electron beam thickness, 0.035 cm, and is centered just outside the cathode radius at 0.37 cm. The diameter of the cylindrical waveguide entrance port in the virtual cathode region is chosen as 1.06 cm, causing the space-charge limited current in this region to drop to 45% of its value in the source region. The ensuing virtual cathode formation drives the production of 50 GHz, 6 mm wavelength microwaves for a 30 kilogauss applied field.

The components of the beam target assembly of Figure 18 are all nominally grounded, with the cathode driven at negative high voltage. In order to diagnose the electron beam operation, however, the anode, annular limiter, and waveguide entrance port are mounted in such a way that, although rigidly attached as a unit, the components are electrically floating. In this way the current to each of the electrodes can be monitored, either by use of a shunt or with a Rogowski coil. Comparing the cathode current to the anode current will then yield an estimate of shank emission and gap closure time; the current to the annular limiter and waveguide entrance port will give an estimate of how well the assembly is centered as well as the beam thickness. These simple beam diagnostics will be supplemented by a Faraday cup current collector mounted on a mechanical probe drive mechanism for making detailed measurements of the electron beam profile.

Magnet Design

The main design criteria for the VIRCATOR magnet are related to field intensity and field homogeneity. The maximum design field is 60 kilogauss, required to drive 100 GHz microwaves in the above experimental configuration. Since diverging magnetic field lines increase beam divergence, magnetic field homogeneity is required in order that the beam particle density at injection into the virtual cathode region be the same as the beam electron density at the source. An additional constraint imposed on the design is that the working magnetic field volume be several times larger in radius and length than the nominal anode size described in the previous section. The magnet has been designed oversize to allow for the contingency that anode-cathode gap closure problems with the nominal 0.08 cm wide gap may require using a much larger anode-cathode radial spacing, of order millimeters. Maintaining diode impedance in the 50 ohm range would then require increasing the anode diameter to centimeters. The present magnet design admits this option.

The magnet overall length is 15.2 cm with a usable inside diameter of 3.5 cm. To produce a 60 kilogauss field on axis at the center of the magnet requires a linear current density of 49,500 amp-turns/cm. The magnet is wound with 284 turns of 1 mm diameter solid copper wire so that the coil current is 2.6 kA and magnet inductance is 1 millihenry. In order to enhance field homogeneity, the coil is wound with additional turns at the ends. The self forces on the magnet tend to squeeze it axially and expand it radially. Self-compression forces in the axial direction are taken up by the copper windings and the epoxy binder, and the radial expansion forces are born by an encapsulating cylindrical stainless steel tube. Neglecting the restoring forces provided by the copper windings and epoxy binder yields a stress of 15,300 psi in the 3.2 mm thick, 6.4 cm outside diameter tube for a 60 kG field. Since the yield strength of type 304 stainless steel exceeds 40,000 psi, the design provides an acceptable safety factor.

The magnetic field risetime is determined by the magnetic inductance, source capacitance, and series resistance. As described in the next section, these were chosen to give a 300 microsecond risetime. Since the field penetration time for the anode, cathode, and the stainless steel magnet casing are all less than 15 microseconds, the magnetic field in the electron beam source region can be accurately calculated using computer codes which neglect eddy-current effects.

3. Electrical Design

The VIRCATOR electrical system consists of the magnet capacitive discharge circuit, the lumped element Blumlein pulse forming line for driving the electron beam, and associated timing and data recording channels. In order to minimize the emission of electromagnetic radiation from the high speed switching circuits, all high voltage components are enclosed in a grounded Faraday cage formed from bronze screen. Additional shielding for the data channels, consisting of five single trace oscilloscopes and recording cameras, is provided by a fully screened instrumentation rack. Because of the limited number of data channels, the generation of a complete data set will require multiple shots. Due to the expected high shot frequency, one every 5 minutes, data acquisition will still be relatively rapid, provided shot reproducibility is acceptable.

Magnet Pulsed Power Supply

A schematic for the circuit which drives the magnetic field coil is shown in Figure 19. A 90 microfarad energy storage capacitor is discharged into the magnetic field coil through a series resistance which is chosen so that the circuit is critically damped. Since the current does not ring, the lifetime of both the capacitors and the magnetic field coil are increased. The price paid is an increase by a factor of approximately 2.5 in the required bank capacitance relative to a lightly damped circuit.

The same result could be achieved by crowbaring the current at peak field with an ignitron, and eliminating the series resistance. Since the cost of the increased capacitance is small compared to the cost of the ignitron and its driving circuit, the former option was chosen.

The magnet energizing circuit of Figure 19 operates as follows. A 20 kv, 10 mA power supply (Del Electronics #RIU-20-10) charges the 90 microfarad capacitor bank to its charge voltage, about 10 kv for a 40 kilogauss field. A krytron gas tube switch is command triggered to discharge a 1 microfarad capacitor charged to 2.5 kv into the ignitor terminals of a mercury ignitron (General Electric #GL-7703). The triggered ignitron then discharges the main capacitor bank into the inductive load through a 6.7 ohm series resistor. The peak magnetic field occurs at 300 microseconds, and decays with a time constant of 300 microseconds. A time delay generator (California Avionics #113CR) command fires a spark gap, initiating the electron beam at peak magnetic field time.

Electron Beam Pulsed Power Supply

The ideal voltage pulse shape for driving the electron beam would have a fast leading edge for initiating field emission at the cathode, followed by a somewhat lower voltage flat top for driving constant current in an assumed constant impedance load provided by the diode. A good approximation to this ideal source is provided by a lumped element artificial Blumlein pulse-forming line shown in Figure 20, which uses high energy density barium titanate capacitors as the energy storage medium. This circuit provides twice the charge voltage into an open load, thereby initiating breakdown at the cathode, followed by an approximately flat top signal equal to the charge voltage when driving a matched load. For a N-stage pulse-line the risetime τ , pulse length T, and impedance Z are given by

ELECTRON BEAM PULSED POWER SUPPLY

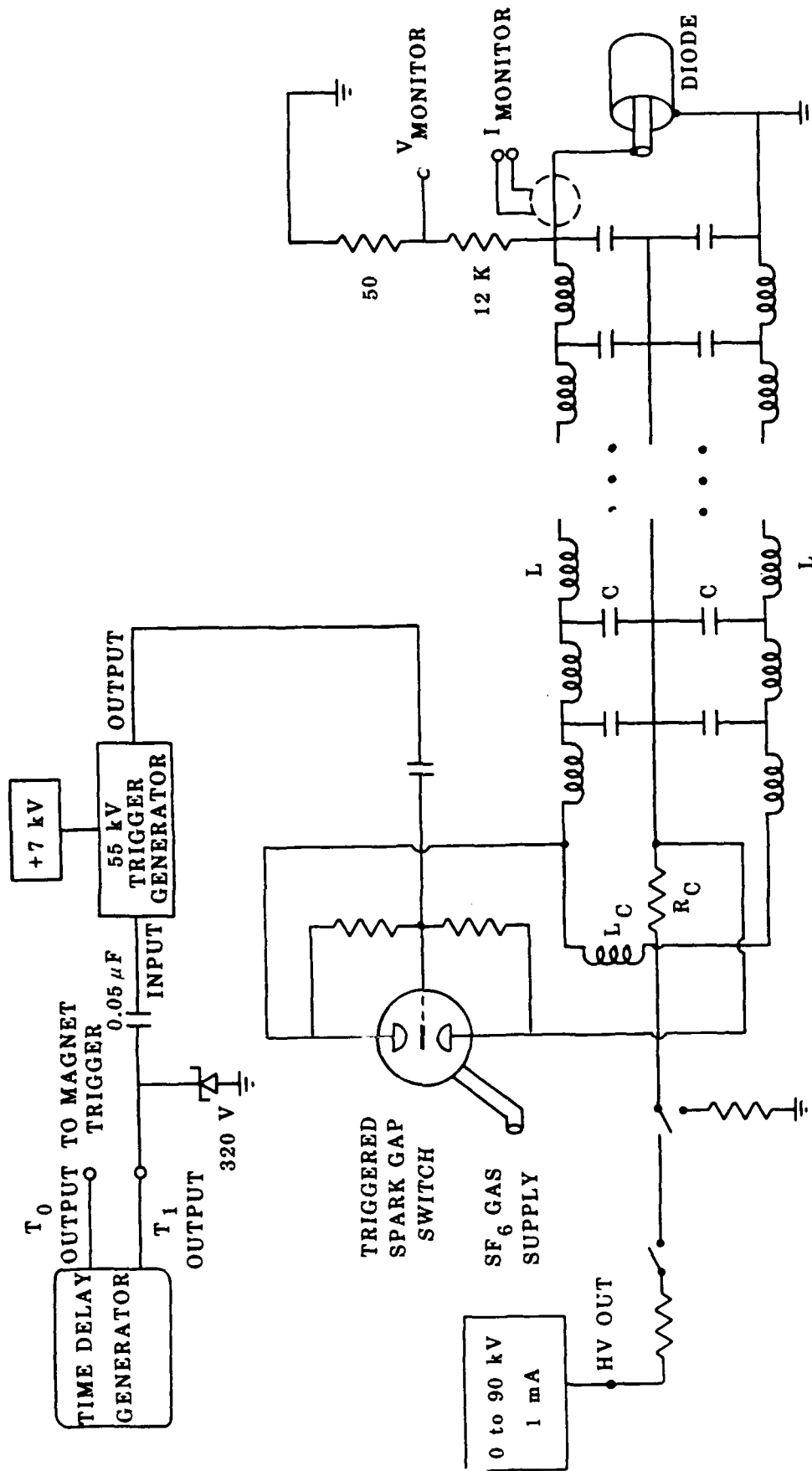


Figure 20. Schematic of the lumped element Blumlein pulse-forming line. Initially 10 stages will be used to give a pulse length of 600 nanoseconds.

$$\tau = \sqrt{LC/2} \quad (57)$$

$$T = 2N\sqrt{LC} \quad (58)$$

$$Z = 2 \sqrt{L/C} \quad (59)$$

where L and C are the component inductances and capacitances, respectively. In order to build in future capability for 100 kV operation, three 40 kV disc capacitors will be connected in series to give 900 pF rated at 120 kV. Matching the pulse-line impedance to the desired diode impedance of 66 ohms requires an inductance of .98 microhenries. For a ten stage pulse forming line the risetime and pulse length follow from above as 15 and 594 nanoseconds, respectively. Increasing the number of stages to provide full 1 microsecond pulse length capability is straight-forward and will be done after any gap closure problems occurring at the shorter pulse lengths have been solved. Increasing the number of stages has an additional benefit of smoothing the flat top portion of the voltage pulse.

The trigger and charging circuit for the electron beam driver are shown in Figure 21. The Blumlein array is charged by a 90 kV power supply (Del Electronics #RIU-90-1-1) and command fired at the time of peak magnetic field by a signal from the time delay generator. The time delay generator triggers a 55 kV pulse generator (Pacific Atlantic Electronics #PT-55-M) which in turn drives the spark gap (Pulsar #670). The spark gap discharges the pulse-forming line into the load provided by the electron beam. A Rogowski coil and voltage divider monitor the diode current and voltage, respectively.

LUMPED ELEMENT BLUMLEIN PULSE-FORMING LINE

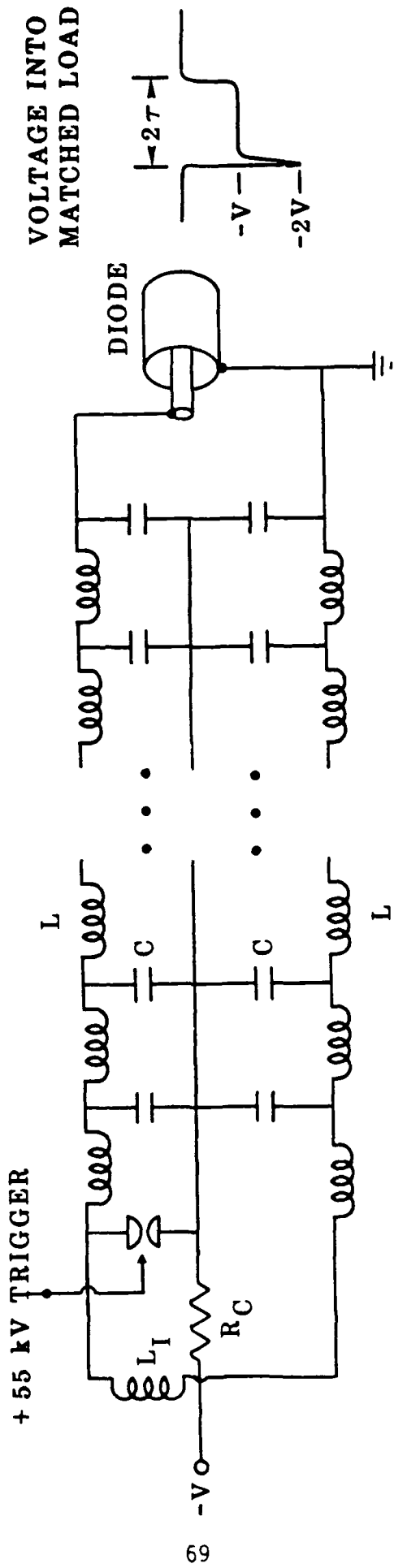


Figure 21. Schematic of the Blumlein charging and trigger circuit which drive the electron beam.

VI. TECHNICAL REQUIREMENTS AND TASKS

HOW THE STATEMENT OF WORK HAS BEEN SATISFIED

In this section we review the tasks encompassed by the statement of work and detail how these technical requirements have been satisfied. We also include a list of publications and talks given on this subject, professional personnel associated with the research effort, and consultative and advisory functions.

Statement of Work (0001AA)

1. Theoretically determine an optimal configuration for a proof-of-principal vircator which operates in the millimeter wavelength regime.

We have reviewed in detail how one can accurately calculate the space-charge limiting current, which is a necessary requirement for determining if a virtual cathode will form, in Section II. For the first time both the nonlinear treatment of the space-charge limit instability and the scaling of key parameters (oscillation frequency, potential depth, location of the virtual cathode) has been accomplished. This is presented in Section III. Work is now in progress on the effect of electron temperature and multiple virtual cathode formation. (See list of proposed publications.)

It is now clear, based on simulations performed at Los Alamos National Laboratory (LANL) and from our analytical efforts that beam temperature not only effects virtual cathode frequency bandwidth, but more importantly microwave generation efficiency. The conclusion of this report that a foilless diode and some means of preventing electron reflexing are optimal for producing a narrowband, efficient oscillator is certainly justified. This work is presented in Section IV.

2. Accomplish the technical design of the proof-of-principle vircator.

The technical design of the vircator is given in Section V. Of greatest importance is the flexibility which is provided by this plan. For instance, the field coil is devised to allow a 60 kG field with an acceptable margin of mechanical safety. Also the artificial Blumlein will allow us to obtain 100 kV pulses, if we used three rather than two barium titanate capacitors per stage.

3. Fabricate portions of the vircator incorporating long lead items.

We have designed the custom bell jar vacuum feedthrough system. It is currently being manufactured. All of the electrical components (capacitors, vacuum feedthroughs, delay generators, switches, and power supplies) have been specified, ordered and delivered. Mechanical components for accurate positioning of the beam-target assembly and raw materials for the assembly have been ordered and delivered. The construction of the Blumlein and assembly will be completed shortly.

4. Design, construct and calibrate a quasi-optical microwave spectrometer.

The design of the spectrometer is presented in Appendix A. It has been constructed. Calibration using high frequency sources available at the Naval Research Laboratory (NRL) will be completed in the month of February. In order to maximize the utility of the spectrometer its current frequency range (75-110 GHz) will be extended down to 35 GHz. This addition will be accomplished by April 1, 1983.

5. Characterize the microwave emission (power, frequency and bandwidth) of a relativistic electron beam in a vircator configuration using the microwave spectrometer.

This last task has not been accomplished. The lack of availability of time on such a beam machine at the Air Force Weapons Laboratory (AFWL) and the longer than anticipated time required to complete task 4, both contributed to this situation. We have postponed this requirement to CY 1983.

Bibliography of Talks and Publications

Archival Scientific Publications

"Design of a Millimeter Wave Source Using a Virtual Cathode Oscillator (VIRCATOR)", in Conference Record - 1982 IEEE International Conference on Plasma Science, p. 54.

"Effects of Temperature on the Space-Charge Limit of Electron Beams", to be submitted to Applied Physics Letters (E. A. Coutsias and D. J. Sullivan).

"Formation of Singularities in One-Dimensional Electron Flows", to be submitted to Physics of Fluids (E. A. Coutsias and D. J. Sullivan).

"High Power Microwave Generation from a Virtual Cathode Oscillator", to be published in IEEE Trans. Nuc. Sci., June 1983 (D. J. Sullivan).

Classified Scientific Reports

"Theory and Design of a High Power Virtual Cathode Oscillator (VIRCATOR)", to be published in Proceedings of the 2nd National Conference on High Power Microwave Technology (D. J. Sullivan).

Internal MRC Reports

"Theory and Application of the Virtual Cathode in Charged Particle Beams," AMRC-R-433 (1982).

Talks and Meetings

1982 IEEE International Conference on Plasma Science, Ottawa, Canada

"Design of a Millimeter Wave Source Using a Virtual Cathode Oscillator (VIRCATOR)"

MGX Review Meeting - Lawrence Livermore National Laboratory (22 Sep 82)

"MGX Simulations Using CCUBE"

Virtual Cathode Microwave Design Review - Los Alamos National Laboratory (31 Jan 83)

"VIRCATOR Theory and Design at Mission Research Corporation"

"The Mission Research Corporation VIRCATOR"

Second National Conference on High Power Microwave Technology - Harry Diamond Laboratories (Mar 83)

"Theory and Design of a High Power Virtual Cathode Oscillator (VIRCATOR)"

1983 Particle Accelerator Conference - Santa Fe, New Mexico

"High Power Microwave Generation from a Virtual Cathode Oscillator (VIRCATOR)"

Professional Personnel (Alphabetical order)

W. Michael Bollen
Evangelos A. Coutsias (UNM Department of Mathematics and Statistics)
Carl A. Ekdahl
Robert H. Jackson
Bret E. Simpkins
Donald J. Sullivan
Donald E. Voss
John Walsh (Dartmouth College, Department of Physics and Astronomy)

Consultative and Advisory Functions

Consulting Agreement with Lawrence Livermore National Laboratory (LLNL) to aid in design of the Microwave Generator Experiment (MGX) which uses a VIRCATOR as the microwave source. Points of contact at LLNL Drs. Hriar Cabayan, Wayne Hohfer, Raymond Scarpetti and George Vogtlin. Dates present at LLNL 25-27 May 1982 and 20-23 September 1982.

Numerous informal discussions with Los Alamos National Laboratories (LANL) personnel in Groups R-1 and X-8 on using the VIRCATOR as a microwave source. In particular discussions with Drs. Carl Ekdahl and Thomas Kwan.

REFERENCES

1. G. D. Child, Phys. Rev. Ser. I 32, 492 (1911).
2. I. Langmuir, Phys. Rev. 21, 419 (1923).
3. C. K. Birdsall and W. B. Bridges, Electron Dynamics of Diode Regions, Electrical Science Series (Academic Press, 1966), Chapter 3.
4. H. R. Jory and A. W. Trivelpiece, J. Appl. Phys. 40, 3924 (1969).
5. V. S. Voronin, Yu, T. Zozulya and A. N. Lebedev, Zh. Tekh. Fiz. 42, 546 (1972), [Sov. Phys.-Tek. Phys. 17, 432 (1972)].
6. R. J. Lomax, Proc. IEE Pt. C 108, 119 (1961).
7. C. E. Fay, A. L. Samuel, and W. Shockley, Bell System Techn. J. 17, 49 (1938).
8. C. K. Birdsall and W. B. Bridges, J. Appl. Phys. 32, 2611 (1961).
9. W. B. Bridges and C. K. Birdsall, J. Appl. Phys. 34, 2946 (1963).
10. D. A. Dunn and I. T. Ho, A.I.A.A.J. 1, 2770 (1963).
11. S. A. Goldstein and R. Lee, Bull. Am. Phys. Soc. 23, 763 (1978).
12. R. A. Meyer, S. A. Goldstein, D. D. Hinshelwood and G. Cooperstein, Bull. Am. Phys. Soc. 24, 977 (1979).
13. D. S. Prono, J. M. Creedon, I. Smith and N. Bergstrom, J. Appl. Phys. 46, 3310 (1975).

REFERENCES (Continued)

14. D. S. Prono, J. W. Shearer and R. J. Briggs, Phys. Rev. Lett. 37, 2 (1976).
15. P. A. Miller, J. A. Halbleib, J. W. Poukey and J. T. Verdeyen, J. Appl. Phys. 52, 593 (1981).
16. J. W. Poukey and N. Rostoker, Plasma Phys. 13, 897 (1971).
17. C. L. Olson, "Collective Ion Acceleration with Linear Electron Beams," in Collective Ion Acceleration-Springer Tracts in Modern Physics, Vol. 84, (Springer-Verlag, 1979).
18. C. L. Olson, IEEE Trans Nuc. Sci. NS-26, 4231 (1979).
19. C. L. Olson, J. R. Woodworth, C. A. Frost and R. A. Gerber, IEEE Trans. Nuc. Sci. NS-28, 3349 (1981).
20. R. B. Miller, in Proc. of the 2nd Intl. Top. Conf. on High Power Electron and Ion Beam Research and Technology, (Cornell University, 1977), p. 613.
21. R. B. Miller, in Collective Methods of Acceleration, edited by N. Rostoker and M. Reiser (Harwood Academic Publishers, 1979), p. 675.
22. R. A. Mahaffey, P. Sprangle, J. Golden and C. A. Kapetanacos, Phys Rev. Lett. 39, 843 (1977).
23. H. E. Brandt, A. Bromborsky, H. B. Bruns, and R. A. Kehs, in Proc. of the 2nd Intl. Top. Conf. on High Power Electron and Ion Beam Research and Technology, (Cornell University, 1977), p. 649.

REFERENCES (Continued)

24. J. M. Buzzi, H. J. Doucet, B. Etlicher, P. Haldenwang, A. Huetz, H. Lamain, C. Rouille, J. Cable, J. Delvaux, J. C. Jouys and C. Peugeot, *idem*, p. 663.
25. D. J. Sullivan, in Proc. of the 3rd Intl. Top. Conf. on High Power Electron and Ion Beam Research and Technology, (Institute of Nuclear Physics, 1979), p. 769.
26. A. N. Didenko, G. P. Fomenko, I. Z. Gleizer, Ya. E. Krasik, G. V. Melnikov, S. F. Pereygin, Yu. G. Shtein, A. S. Sulakshin, V. I. Tsvetkov, and A. G. Zerlitsin, *idem*, p. 683 (1979).
27. L. A. Bogdankevich and A. A. Rukhadze, *Soviet Phys. Uspekhi*, 14, 163, (1971).
28. B. N. Brejzman and D. C. Ryutov, D. C., *Nucl. Fusion*, 14 875, (1974).
29. T. C. Genoni and W. A. Proctor, 1978 IEEE Conf. on Plasma Sciences, Poster Session 2P1.
30. R. B. Miller and D. C. Straw, *J. Appl. Phys.*, 47, 1897, (1976).
31. J. R. Thompson and M. L. Sloan, Proceedings of the 2nd International Conference on High Power Electron and Ion Beam Research and Technology, Vol. II, p. 734, Eq (14), Laboratory for Plasma Studies, Cornell University, Ithaca, New York, October 3 - 1977.
32. D. B. Godfrey, *J. Comp. Phys.*, 15, 504 (1974).
33. B. P. Godfrey, *J. Comp. Phys.*, 19, 58 (1975).

REFERENCES (Continued)

34. R. B. Miller and D. C. Straw, J. Appl. Phys., 48, 1061 (1977).
35. L. E. Thode, B. R. Godfrey and W. R. Shanahan, Phys. Fluids, 22, 747 (1979).
36. R. Z. Sagdeev, Reviews of Plasma Physics, Vol. 4, edited by M. A. Leontovich, (Consultants Bureau, 1966), p. 23.
37. S. S. Moiseev and R. Z. Sagdeev, Plasma Phys. 5, 43 (1963).
38. G. B. Whitham, Linear and Nonlinear Waves, (Wiley, 1974).
39. E. A. Coutsias and D. J. Sullivan, to be submitted to Physics of Fluids.
40. D. J. Sullivan and E. A. Coutsias, in High Power Beams '81, edited by H. J. Doucet and J. M. Buzzi, (Ecole Polytechnique, 1981), p. 371.
41. J. R. Pierce, J. Appl. Phys. 15, 721 (1944).
42. J. W. Poukey, J. P. Quintenz and C. L. Olson, Appl. Phys. Lett. 38, 20 (1981).
43. B. B. Godfrey, Mission Research Corporation, AMRC-R-282 (1981), unpublished.
44. J. Kevorkian and J. D. Cole, Perturbation Methods in Applied Mathematics, (Springer, 1981).
45. G. Birkhoff and G. Rota, Ordinary Differential Equations, (Ginn and Company, 1962).

REFERENCES (Continued)

46. A. V. Paschenko and B. N. Rutkevich, *Fiz. Plazmy* 3, 774 (1977), [*Sov. J. Plasma Phys.* 3, 437 (1977)].
47. A. Bromborsky, H. Brandt, and R. A. Kehs, *Bull. Am. Phys. Soc.*, 26, 165 (1981); and private communication.
48. D. J. Sullivan, *Bull. Am. Phys. Soc.*, 25, 948 (1980).
49. M. E. Jones and L. E. Thode, *J. Appl. Phys.*, 51, 5212 (1980).
50. R. B. Miller, K. R. Prestwich, J. W. Poukey, and S. L. Shope, *J. Appl. Phys.*, 51, 3506 (1980).
51. R. Prohaska and A. Fisher, *Rev. Sci. Instr.* 53, 1092 (1982).

APPENDIX A

MRC/WDC-R-046

TECHNICAL REPORT

A W-BAND DIFFRACTION GRATING SPECTROMETER

W. Michael Bollen
R. H. Jackson

December 1982

Prepared for: Air Force Office of Scientific Research
Physics Directorate
Bolling Air Force Base, DC 20332

Under Contract: F49620-82-C-0014

Prepared by: MISSION RESEARCH CORPORATION
5503 Cherokee Avenue, Suite 201
Alexandria, Virginia 22312

SECTION 1 INTRODUCTION

1.1 Background

In characterizing electromagnetic radiation, the intensity and wavelength of the radiation are used. A device for measuring these two quantities is the spectrometer. Spectrometers are a commonly used device in the UV, visible and IR region of the spectrum. A variety of techniques for performing the spectrometry may be used: Fabry-Perot interferometry, Fourier transform spectroscopy, and diffraction grating spectroscopy. For the microwave spectrum, the Fourier transform technique, commonly called a spectrum analyzer, has been used. The other methods have not had widespread use with microwaves.

Spectrometry for non-repetitive, short pulse length microwave radiation can only be easily performed using the grating spectrometry method mentioned above, and it has been used with some success^{2,3,4}. The main difficulty encountered has been in calibration of the spectrometer. Calibration is required because the response typically is not flat; the signal output varies with wavelength for a constant intensity input. Further, calibration sources are not easily available except at very low power levels (milliwatts). In our design we have attempted to make the response flat; however, we are limited by the nonuniform response of the microwave detectors.

1.2 The Diffraction Grating Spectrometer

A basic description of diffraction grating spectrometers can be found in many optics texts (see, for example, reference 5). The physics of the diffraction process is described by

$$m\lambda = d(\sin\alpha \pm \sin\beta) \quad (1)$$

where m is the order of the diffraction ($0, \pm 1, \pm 2, \dots$), λ is the wavelength, d is the spacing between the grating grooves, α and β are the angles of incidence and diffraction respectively (see Figure 1). The plus sign is used in equation 1 if α and β are the same sides of the surface normal; otherwise, the minus sign is used. Figure 1 depicts the commonly used echelette grating (ninety degree apex angles). The echelette is popular because it is easy to fabricate, and it has been shown experimentally to give the best efficiency for a ruled grating.

The dispersion of the grating (for fixed incident angle, α) is expressed as

$$d\beta/d\lambda = m/(d \cos \beta) \quad (2)$$

where terms are defined as before. The resolving power, R , is

$$R = \lambda/\Delta\lambda = mN \quad (3)$$

where N is the number of grooves; however, there is a fundamental limitation on R ,

$$R \leq 2W/\lambda \quad (4)$$

where W is the width of the grating ($W = Nd$). The details of our design using these equations may be found in the next section.

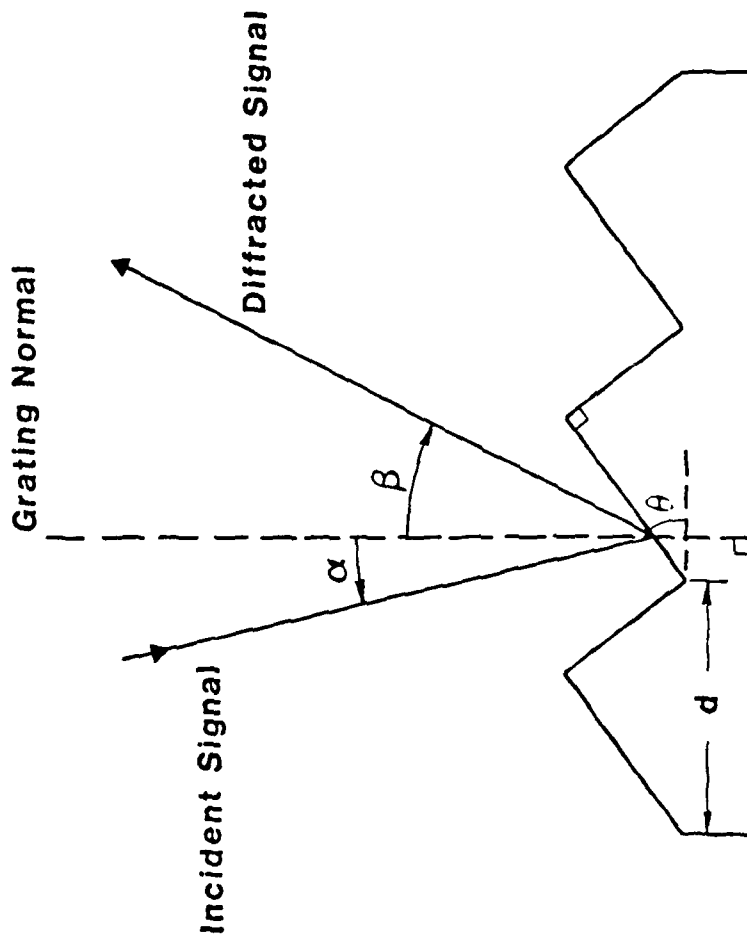


Figure 1. Definition of geometry for an Echelle grating.

SECTION 2 DESIGN OF A W-BAND SPECTROMETER

2.1 Design Philosophy

A microwave spectrometer has been designed to measure frequency and bandwidth for radiation from the Mission Research Corporation (MRC) vircator experiment. An effort has been made to improve upon the basic design currently in use^{2,3,4} by incorporating new knowledge on diffraction gratings⁶ and by the use of innovative design concepts. Computational modeling suggests 3-4 mm radiation from the vircator with fine structure of 2 GHz. These were used as the basic design constraints. Additionally, we imposed the following constraints to make the device easier to use: 1) limit the wavelength range to remove high order ($m > 1$) diffraction, 2) demand uniform (flat) device response, 3) require wide device bandwidth, 4) require wide bandwidth for any single input pulse, 5) allow for modification to different wavelength bands, 6) minimize unwanted signal noise, and 7) keep the device small and portable. Clearly, all these constraints can not be simultaneously met, and trade-offs were required.

The final design is shown in Figure 2. This spectrometer is designed to operate at W band (2.7-4 mm) with a minimum of 2 GHz resolution over the entire band. The bandwidth of the device is limited on the long wavelength end by the W-band input waveguide, and on the short wavelength end by the low-pass diffraction grating. This effectively eliminates higher-order ($m > 1$) diffraction. Care was taken in the design of the diffraction gratings to choose a design with a flat frequency response. The main limitation encountered in obtaining uniform response was in the microwave detectors. These do not have uniform response, and their response varies with each detector. Wide device bandwidth is obtained by the use of a rotatable diffraction grating. Wide, single-shot bandwidth is obtained by using a large reflection mirror (allowing for more than one diffraction angle) and use of a multichannel detection array. We have chosen a six-channel detection array designed for 10 GHz

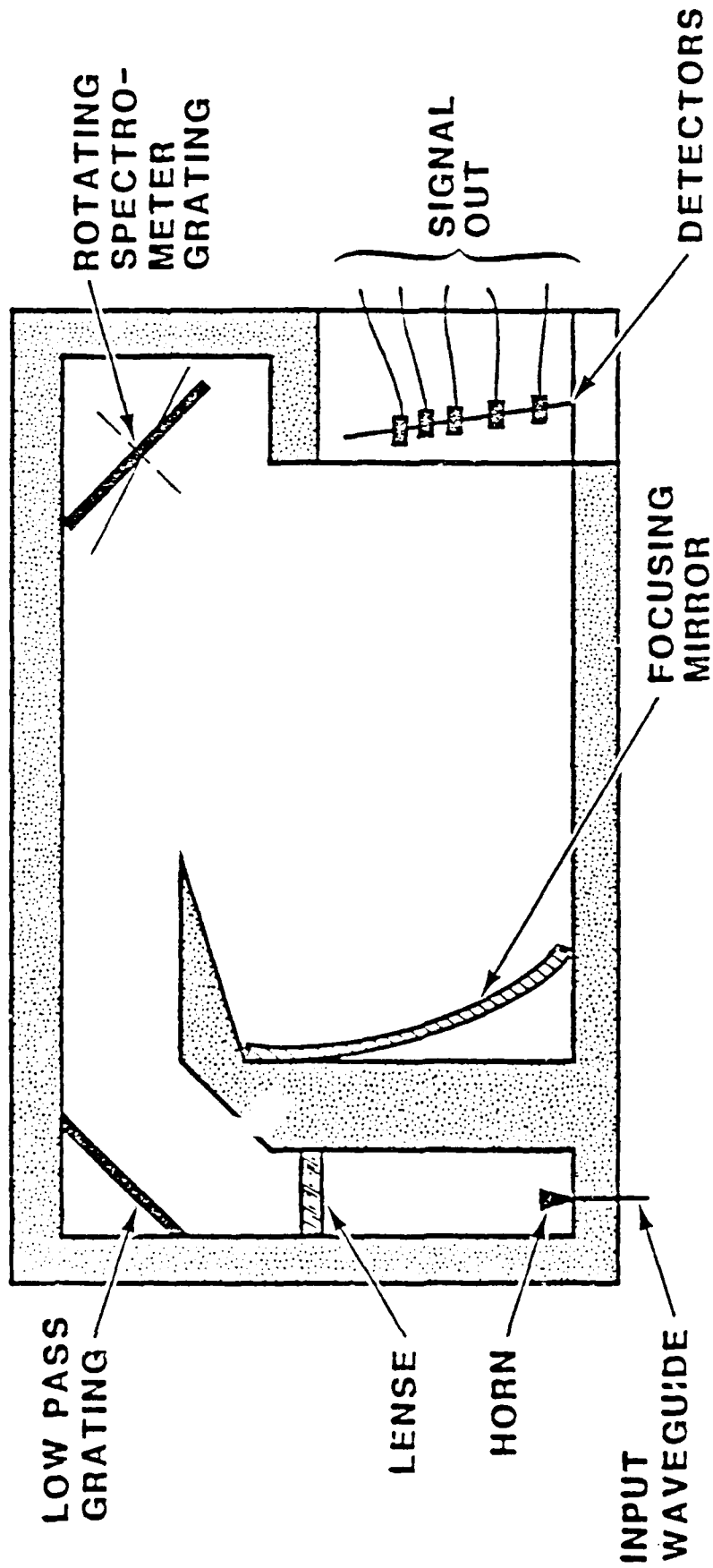


Figure 2. The MRC W-band spectrometer.

full-width band response centered at 4 mm (75 GHz). Modification to different bands is possible by replacing the two diffraction gratings. Where possible, device size was reduced. For example, folding of path length was done. Path length folding and use of microwave absorber also removed any direct line of sight between the initial input signal and the diffracted signal detectors. Additionally, a collimating horn/lense system was used allowing a slight savings in size over that achieved using a mirror system. The details concerning the design of individual components is found in the next section.

2.2 Design of the MRC W-Band Spectrometer

2.2.1 Microwave Input

The microwaves enter the spectrometer through a length of W-band waveguide (see Figure 2). The waveguide performs the first filtering by rejecting microwave wavelengths greater than 4 mm. The input signal must be attenuated to a level of a few hundred milliwatts to prevent damage to the microwave detectors. Some attenuation (10-20 dB) will occur in the spectrometer itself (due to losses); however, the main attenuation must be performed externally. This is performed geometrically by moving the input of the waveguide away from the output of the microwave source; then geometrical, $1/R^2$, attenuation will occur. A 10 MW signal will be attenuated to 100 mW in the waveguide input for a separation, R, of 10 meters.

Geometrical attenuation assumes a uniform distribution of the microwaves over a spherical surface (actually half of the surface for our case). The accuracy of this assumption depends on two factors. First, the spectrometer must be located in the far field;

$$R \geq D^2/\lambda \quad (5)$$

where D is the diameter of the source aperture, λ is the wavelength of the radiation, and R is the separation distance. For most cases of interest to us, this is usually easily satisfied. For example, for a 1 cm wide output aperture at 4 mm, the separation must be 2.5 cm. Second, a TE_{11} mode (dominant mode) in circular waveguide has been assumed. Other modes can cause the distribution of power to be peaked at certain angles. For this reason, a mapping of the angular power distribution should be performed. If it is not uniform, then the spectrometer measurements should be made at several angles. It is conceivable that the frequency of the microwaves from the source is linked to the mode. Thus, a measurement of the entire spectrum requires a sampling of all modes.

Inside the spectrometer the input signal is expanded using a standard gain, rectangular horn. This horn has a beam width (FWHM) of 20° . A collimating lense is placed in the far field of the horn and at a distance such that half of the input signal is intercepted. The lense is a standard hyperbolic design.⁷ The front surface is hyperbolic in shape and is described mathematically by

$$R = \frac{(n - 1) L}{n \cos \theta - 1} \quad (6)$$

where n is the index of refraction and R , L , and θ are shown in Figure 3. The lense is made from Rexolite ($n = 1.6$). Rexolite has a large index of refraction and low attenuation for millimeter microwaves.⁸ The horn/lense collimation technique is compact and aids in reducing the overall size of the spectrometer.

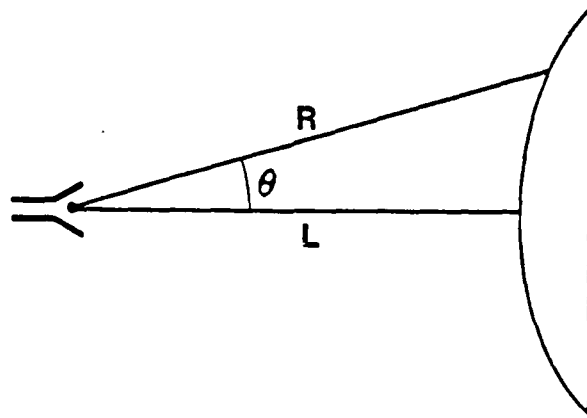


Figure 3. The geometry used for determining the surface of a hyperbolic lens.

2.2.2 Diffraction Grating

Although the basic theory of diffraction gratings has already been discussed in Section 1.2, a few more definitions are required. When discussing gratings, the typical mount used is the Littrow mount. For this case, the incident and diffracted rays occur on the same line ($\beta = -\alpha$). Under these conditions equation (1) simplifies

$$m\lambda = 2d \sin \alpha . \quad (7)$$

Further, if the angle of the grooves, θ (see Figure 1), is the same as α , maximum diffraction will occur since the diffracted and reflected angles are the same. This condition is referred to as being "in blaze" and θ is the blaze angle. The Littrow mount is obviously not realizable in actual practice; however, for TM radiation (H parallel to the grooves), a departure from Littrow still yields a high and nearly uniform efficiency, provided that $0.85 \leq \lambda/d \leq 1.5$. This is true up to 45° off Littrow. Therefore, the gratings were designed using TM radiation and assuming a Littrow mount. An Echelette grating design was chosen and a blaze angle of 30° was picked. For this blaze angle, nearly uniform transmission occurs for $.7 \leq \lambda/d \leq 1.7$ (see Figure 4)⁶. From Figure 4 it is clear that the grating operates best for $1 \leq \lambda/d \leq 1.5$. This fixes d for the grating. The grating characteristics are shown in Table 1. In order to use a rotating diffraction grating, the angle $\alpha - \beta$ was fixed. The detectors and collecting mirror can then be fixed with respect to the incoming microwaves, and the frequency is scanned by rotating the grating. In our design $\alpha - \beta$ is set equal to 25° . This angle is kept as small as possible to stay near Littrow, but must be made large enough so the reflecting mirror does not occlude the diffraction grating.

In addition to the diffraction grating which disperses the microwaves for wavelength measurements, another grating is used in the zeroth order ($m = 0$) to limit the wavelength of the radiation to the dispersing grating. It can be shown⁶ that a grating acts like a mirror in $m = 0$ for sufficiently large wavelength radiation. The criteria is

$$d < \lambda_{\min}/(1 + \sin \alpha) \quad (8)$$

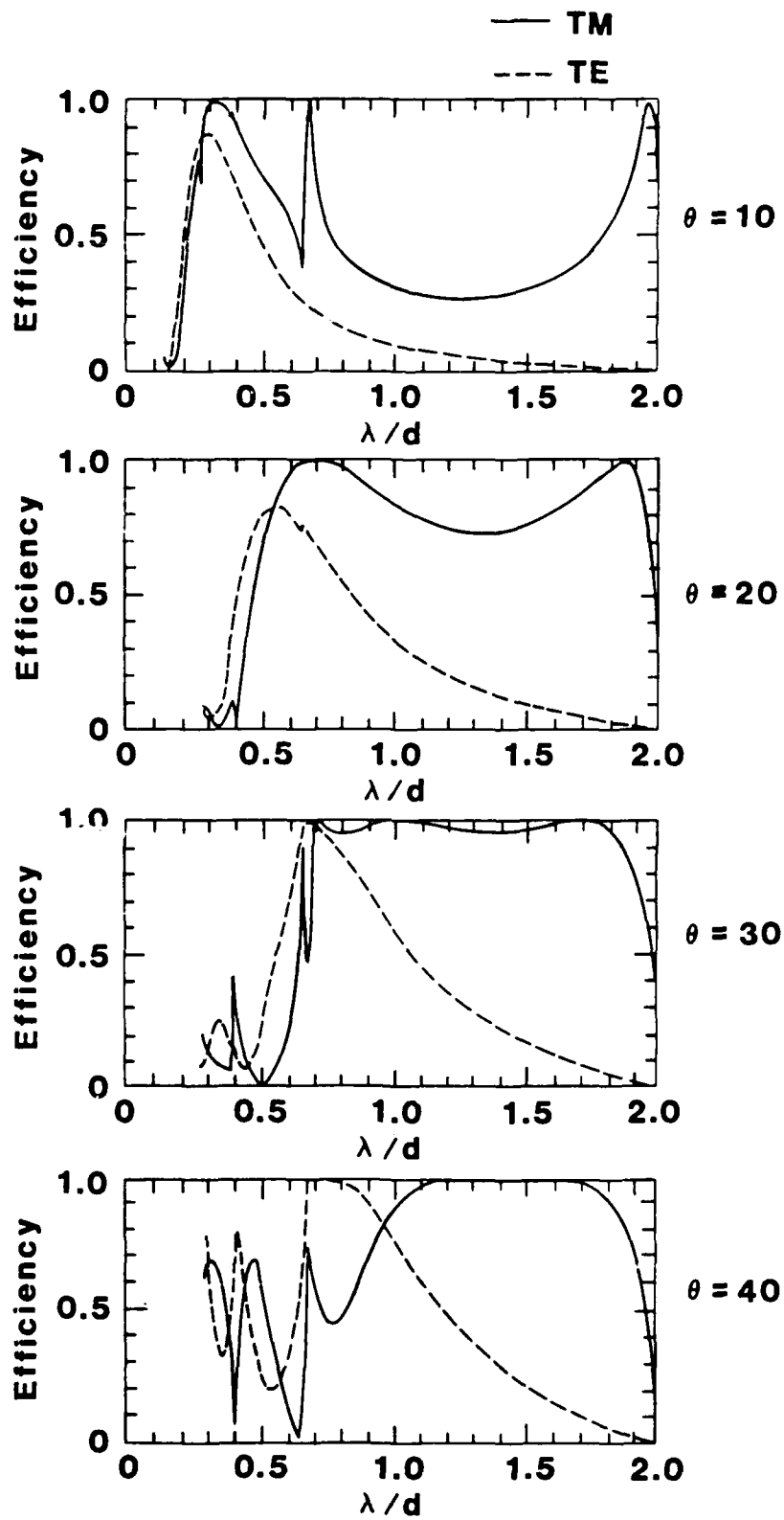


Figure 4. Efficiency of Littrow mount Echelle gratings with blaze angle θ . The solid line is TM polarization (H parallel to grating grooves) and the dashed line is TE polarization (E parallel to grating grooves).

TABLE 1

F	λ/d	α	β
110	1.01	43.65	18.50
100	1.11	47.2	22.2
90	1.24	52.0	27.0
80	1.39	58.0	33.0
75	1.48	61.85	36.85

F is frequency

α is angle of incidence

λ is wavelength

β is angle of diffraction

d is groove spacing

refer to Figure 1 for definition of geometry

For the grating

$d = 0.27$ cm

$\theta = 30^\circ$ (Note: The grating is also in blaze for $90 - \theta = 60^\circ$)

α and β are computed based on $\alpha - \beta = 2\theta_D = 25^\circ$.

where λ_{\min} is the shortest wavelength for which the grating will act as a mirror. We chose α equal to 45° and λ_{\min} equal to 2.2 mm (140 GHz). Using this grating as a reflecting mirror effectively removes the possibility of higher order radiation appearing on our detectors. (For example, 2 mm radiation for $m = 2$ will appear the same as 4 mm radiation for $m = 1$.) The mirror/grating then reflects all radiation with a wavelength greater than 2.2 mm and diffracts all shorter wavelength radiation. We have placed microwave absorbers in the proper position to remove the diffracted short wavelength radiation.

2.2.3 Diffracted Signal Detection

As mentioned before, a multichannel detection system was decided upon to give broadband response on a single-shot basis. It was decided to design for a 10 GHz bandwidth centered at 75 GHz (4 mm). The detection system consists of six microwave detectors. A spherical mirror is used to concentrate the diffracted radiation. The mirror and detector locations were designed graphically using ray tracing. The mirror is 55 cm wide and has a 200 cm radius of curvature. The detectors are located on a focal line which is approximately 100 cm from the mirror. The mirror itself is made using thermoform plastic. A wooden master is machined. The plastic is then formed to the master and coated with a silver, high-conductivity paint.

The actual signal detection is performed using 1N53 diode crystals mounted in W-band waveguide. Although these detectors are not as flat in response as others, their response is not sufficiently poor to justify the increased expense of more uniform response detectors. Expense becomes an important factor due to the potentially short lifetime of the detector. A large microwave signal permanently destroys the crystal. It has been our experience in high-power microwave diagnostics that diode crystals are continually being burned out. This is due to the large power fluctuations that occur in the experimental microwave sources. Due to

this non-uniform response each detector will have to be individually calibrated for frequency response. The output of the detectors will be available on 50 ohm BNC connectors located on the outside of the spectrometer. If long cables will be used, it is recommended that line driver amplifiers also be used.

REFERENCES

1. Gebbie, H. A., "Fourier Transform vs. Grating Spectroscopy," Applied Optics 8, 501 (Mar 1969).
2. Pasour, J. A., "Reflection of Electromagnetic Radiation for the Front of a Magnetically-Confining, Relativistic Electron Beam," Thesis - North Carolina State University at Raleigh, Dept. of Physics 1977.
3. Felch, K. and L. Vallier, "Calibration of a Millimeter Microwave Grating Spectrometer: 55-350 GHz," Report PMI 1052, Laboratoire de Physique des Milieux Ionises, Ecole Polytechnique (Aug 1980).
4. Gold, S. H., W. M. Black, R. H. Jackson, V. L. Granatstein, H. P. Freud, P. C. Efthimion, and A. K. Kinkead, "Study of Emission Spectrum in a Millimeter-Wave Free-Electron Laser Operating in the Collective Regime," Bull. Am. Phys. Soc. 27, 1092 (Oct 1982).
5. Madden, R. P. and John Strong, "Diffraction Gratings," in Concepts of Classical Optics, Appendix P, W. H. Freeman and Co., San Francisco, CA, 1958.
6. Petit, R. ed., Electromagnetic Theory of Gratings, Springer-Verlog, New York, NY, 1980.
7. Kraus, J. D. and K. R. Carver, Electromagnetics, 2nd Ed., McGraw-Hill, Inc. New York, New York, p. 685, (1973).
8. Breeden, K. H. and A. P. Sheppard, "Millimeter and Submillimeter Wave Dielectric Measurements," The Microwave Journal, p. 59, (Nov. 1967).